Statement: An edited version of this paper was published by AGU. Published (2026) American Geophysical Union.

Citation: Yang, G., Rosenau, M., Yin, H., Pan, S., & Pei, Y. (2026). How pre-existing strength heterogeneities and differential extension shaped rift initiation and propagation in the South China Sea: An analog perspective. Journal of Geophysical Research: Solid Earth, 131, e2025JB033244. https://doi.org/10.1029/2025JB033244

How pre-existing strength heterogeneities and differential extension shaped rift initiation and propagation in the South China Sea: An analogue perspective

Gengxiong Yang[1, 2, 3*], Matthias Rosenau[4], Hongwei Yin[3], Shuxin Pan[5], Yangwen Pei[1, 2]

[1]State Key Laboratory of Deep Oil and Gas, China University of Petroleum, Qingdao, China

[2]School of Geosciences, China University of Petroleum, Qingdao, China

[3]School of Earth Science and Engineering, Nanjing University, Nanjing, China.

[4]GFZ - Helmholtz Centre for Geosciences, Potsdam, Germany

[5]Key Laboratory of Reservoir Characterization, Research Institute of Petroleum Exploration and Development-Northwest, PetroChina, Lanzhou, China

Corresponding authors: Gengxiong Yang (yanggx@smail.nju.edu.cn)

Key Points:

- V-shaped rift formed before spreading, controlled by differential extension and crustal strength heterogeneities.
- Differential extension governed rift timing and propagation, while inherited strength heterogeneities controlled the location and geometry.
- Continental basement blocks localized rifts, and also generated troughs and oblique shear faults.

Abstract

Continental rifting rarely occurs synchronously along strike and with uniform width. Instead, it commonly involves diachronous, progressive opening and rift propagation resulting in V-shaped rifts. Rotational, scissor-like opening is a common model explaining V-shaped rifts near plate tectonic rotational poles with steep extension gradients along-strike. However, the mechanisms driving V-shaped rifts located far from such poles, such as the South-China Sea (SCS), remain less well understood. Here, we use crustal-scale analog modeling to investigate the processes and mechanisms of V-shaped rift formation in regions distant from rotational poles, taking the SCS as a prototype. Our results demonstrate that the V-shaped opening of basins can be governed by the combined effects of differential extension and inherited strength heterogeneities in the lithosphere. Applied to the SCS, our models indicate that along-strike variations in Proto-SCS subduction drove spatially variable extension, producing east-to-west diachronous rift initiation and contrasting crustal-thinning patterns between the eastern and western segments. In addition, weak remnants of Mesozoic magmatic arcs in the eastern segment and strong, pre-existing continental basement blocks in the western segment acted as key structural-rheologic controls on strain localization, shaping the geometry of the basin and regulating the degree of necking along the continent–ocean boundary. Collectively, these processes produced the east-ward younging and narrowing V-shaped rift represented by the SCS today. These findings provide new insights into the debated origin of the SCS in particular and broadens our understanding of rift propagation in settings distant from rotational poles in general.

Keywords: V-shaped basins, rift propagation, crustal heterogeneity, differential extension, analog modeling, South China Sea

Plain Language Summary

The South China Sea (SCS) is characterized by westward-propagating rifting and seafloor spreading, which produced a distinctive V-shaped oceanic basin. Because this geometry developed far from the relevant Euler poles, it cannot be readily explained by a simple rotational opening model. Instead, the progressive opening of the SCS likely reflects the combined effects of Cenozoic tectonic forcing and Mesozoic inherited lithospheric structures. Using analog modeling, we explored multiple factors that may have governed the V-shaped configuration of the SCS: (1) variations in extension rate from east to west, driven by unequal subduction of the Proto-SCS, and (2) inherited geological features, including remnant Mesozoic magmatic arcs in the east and continental basement blocks in the west. The results indicate that higher extension rates in the east led to earlier deformation and localized strain along a weak zone related to a remnant magmatic arc, producing a wide and deep rift. In contrast, strain in the west was focused between pre-existing continental basement blocks, generating narrow and deep rift zones. All these processes combined produced an east-wide, west-narrow V-shaped rift. These findings provide new insights into the geological interactions that shaped the SCS and other V-shaped rifts far from rotation poles.

1 Introduction

Rifts are the manifestation of localization of regional horizontal stretching of the continental lithosphere. They are directly related to the complete geodynamic sequence through which the continental lithosphere evolves from initial extension and thinning to rupture and subsequent seafloor spreading, as well as to the inherited transitions among these stages (McKenzie, 1978; Huismans and Beaumont, 2011; Li et al., 2011; Li et al., 2012; Brune et al., 2014). This sequence constitutes a key component of the Wilson cycle (Ding, 2021). Their evolution includes along-strike propagation of rift opening reflected in basin histories. Accordingly, the propagation trajectory of rifting and the gradient in extension rate can exert a significant control on the subsidence pattern, fault-system geometry, and thermal evolution of rifted-margin basins (Ranero and Pérez-Gussinyé, 2010; Xie et al., 2015), thereby further influencing key petroleum geological elements, including the distribution of sedimentary facies belts, hydrocarbon migration and accumulation, and the timing windows of hydrocarbon generation and reservoir formation (Zhang et al., 2020; Pérez-Gussinyé et al., 2024).

Continental rifting is generally regarded as a manifestation of regional horizontal stretching and is commonly attributed to orthogonal or oblique extension in many modeling studies (Clifton & Schlische, 2001; Duclaux et al., 2020). Yet, such mechanisms alone cannot fully explain rift propagation, which produces along-strike structural gradients, diachronous rift development, and ultimately V-shaped basins (Brune et al., 2023; Van Wijk & Blackman, 2005; Zwaan et al., 2020). V-shaped geometries have been linked to rotational (“scissor-like”) divergence near poles of plate tectonic rotation, causing pronounced along-strike extension gradients (Maestrelli et al., 2020; Mondy et al., 2018; Molnar et al., 2017). V-shaped basins may also arise from lateral rheological variations or interactions between propagating basins (Glerum et al., 2020; Gouiza & Naliboff, 2021; Le Pourhiet et al., 2017). However, these models do not adequately account for V-shaped basins that developed far from rotation poles where extension gradients are low and within tectonically complex settings, such as the South China Sea (SCS) (Figure 1a) which serves as a prototype of such basins.

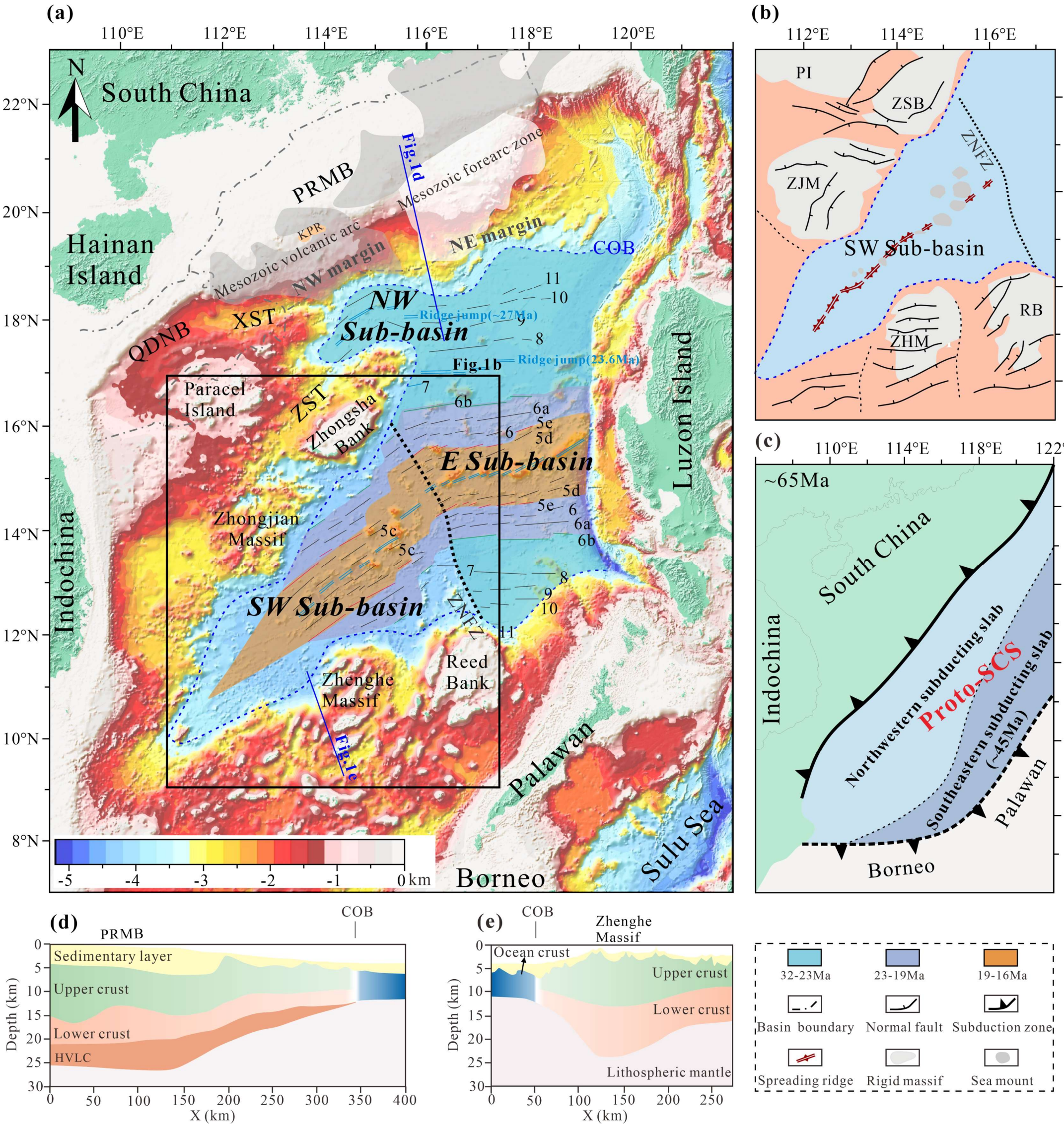

Figure 1. Morphological features of the South China Sea and factors potentially influencing its V-shaped opening. (a) Magnetic lineations overlaid on bathymetric data projected with the pole of opening of stage 1 located 9° N, 65° E (Briais et al., 1993). Location of the remnant Mesozoic magma arc (gray) and forearc basin (white) in the northern SCS after Li et al. (2018) and Zhao et al. (2019). Kaipin Rift (KPR) refers to Xu et al. (2024). (b) Distribution of basement massifs along the continental margin, modified from Ding & Li (2016). (c) Sketch map illustrating the proportion of proto-South China Sea subduction toward the northwest and southeast, modified from F. C. Li et al. (2020). (d, e) Representative profiles of the eastern and western segments, modified from Yan et al. (2001) and Qiu et al. (2011), respectively. QDNB, Qiongdongnan Basin; PRMB, Pearl River Mouth Basin; XST, Xisha Trough; ZNFZ, Zhongnan Fracture Zone; COB, Continent–ocean boundary; ZST, Zhongsha Trough;

ZJM, Zhongjian Massif; ZSB, Zhongsha Bank (Macclesfield Bank); ZHM, Zhenghe Massif; RB, Reed Bank; PI, Paracel Islands (Xisha Islands). Proto-SCS, Proto–South China Sea.

The opening of the SCS was diachronous, propagating from east to southwest (Figure 1a) (Franke et al., 2014; Luo et al., 2021; Pubellier et al., 2022). Specifically, the eastern sub-basin (ESB; Figure 1a) developed between 33 and 15.5 Ma, whereas the southwest sub-basin (SWSB; Figure 1a) formed later, between 23 and 16 Ma (Li et al., 2014). As a result, the present-day oceanic basin exhibits a V-shaped configuration that is wide in the east and narrow in the west. According to magnetic anomaly stripe analyses, the Euler rotation pole of the South China Sea is located at ~9°N, 65°E (Briais et al., 1993; Sibuet et al., 2016; Le Pourhiet et al., 2018) at a distance > 5000 km from the SCS rendering classic scissor-like opening kinematics unlikely. Moreover, along-strike variations in lithospheric stretching indicate that the eastern margin of SCS underwent less extension and display a narrower zone of crustal thinning, whereas the western margin experienced broader and more intense thinning (Huchon et al., 2001; Hayes & Nissen, 2005; Le Pourhiet et al., 2018). This phenomenon is inconsistent with the classical scissor-like opening expected for Euler pole–controlled rotational kinematics. Le Pourhiet et al. (2018) investigated the role of far-field stresses imposed by the stationary Indochina block in shaping SCS rift propagation through 3D numerical simulations. By applying basin-axis normal compression along the western SCS margin, they proposed that the west-to-east topographic gradient across the Indochinese Peninsula stalls westward propagation of breakup, ultimately resulting in V-shaped spreading (Figure 2a). Additionally, previous modeling studies have emphasized the role of relatively strong continental basement blocks (Figure 1b) in resisting the westward rift propagation, whether the blocks were considered distinct entities (Ding & Li, 2016; Figure 2c) or remained connected (Qing et al., 2024; Figure 2b) prior to rifting.

The aforementioned studies in summary attribute the V-shaped opening of the SCS to buttressing-induced far-field compression and to the more local blocking effect of pre-existing continental basement blocks, both of which impeded westward propagation. In addition, geochemical and isotopic evidence indicates that mid-ocean ridge basalts (MORBs) from the SCS record plume–ridge source mixing beginning at ~23.8 Ma (Yu & Liu, 2020). This temporal correspondence suggests that the ridge jump and subsequent seafloor spreading at ~23.6 Ma (Li et al., 2014) may have been plume-related. Seismic structural evidence further indicates that mantle upwelling beneath the northern SCS likely interacted with the overlying crust (Lin et al., 2025). Previous studies have also emphasized the role of remnant Mesozoic magmatic arcs in (Figure 1a) controlling the location of breakup and the style of crustal thinning in the northern SCS (Li et al., 2018; G. X. Yang et al., 2025a; Zhao et al., 2019; Zhang et al., 2023). Yet, most of this research has focused on the north–south transition from continental to oceanic lithosphere, while the potential role of these arcs in east–west rift propagation and interactions with other controlling factors remains poorly constrained (Figure 2c).

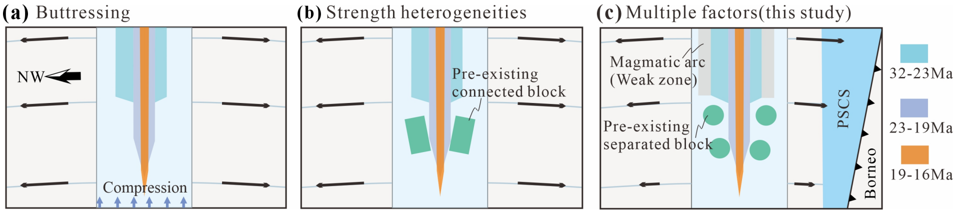

Figure 2. Potential factors controlling the V-shaped opening of the South China Sea. (a) Buttressing model of Le Pourhiet et al. (2018) where far field compression stalls SCS rift propagation (b) Strong block model by Qing et al. (2024) where strength heterogeneities resist propagation. (c) Schematic illustration of the key factors influencing SCS rift propagation that are incorporated into our analog modeling.

Here we add to the discussion and investigate the potential additional effect of an along-strike gradient in extension related to differential subduction of the proto–South China Sea (PSCS) to the south. Geological reconstructions suggest that southeast-dipping PSCS subduction progressively increased eastward in the velocity and amount of subduction (Madon et al., 2013; Figure 1c). F. C. Li et al. (2020) used 2D thermo-mechanical modeling to examine how variations in northward subduction duration influence the SCS's continental breakup styles. Similarly, Larvet et al. (2023) employed 2D numerical simulations to model the effects of PSCS’s southward subduction on SCS opening. However, their work primarily focuses on the mechanical conditions (e.g., age and strength) required for PSCS subduction to contribute to SCS formation, without considering the three-dimensional variability in subduction velocity and amount of the PSCS. Consequently, the potential influence of scissor-like PSCS subduction (Figure 2c) on the V-shaped opening of the SCS remains to be demonstrated.

In this study, we incorporate the effects of Cenozoic differential subduction of the PSCS together with Mesozoic tectonic inheritance, including weak remnant magmatic arcs and previously emphasized strong continental basement blocks (Ding & Li, 2016; Qing et al., 2014) (Figure 2c). Through a series of single-factor and multi-factor analog models, combined with quantitative analyses by means of Particle Image Velocimetry (PIV) and Digital Elevation Models (DEMs), we systematically assess the relative contributions and hierarchical roles of these factors in controlling the V-shaped opening of the SCS. This study advances the understanding of the geodynamic processes that controlled the V-shaped development of the SCS and similar basins worldwide.

2 Geological setting

The SCS is the largest marginal sea in the western Pacific, and has long been a focus of global geological research owing to its unique tectonic setting and its potential oil and gas resources (Savva et al., 2014). The tectonic evolution of the SCS has been widely linked to the southeastward subduction of the PSCS beneath Borneo (Hall, 2002; F. C. Li et al., 2020; Mazur et al., 2012; Wu & Suppe, 2018). Some studies propose that the PSCS was a back-arc extensional basin associated with the rollback of the Paleo-Pacific during the Late Cretaceous (Bai et al., 2015; Morley, 2012; Zahirovic et al., 2014). Tectonic reconstructions indicate that subduction of the PSCS initiated along the South China margin (northward subduction) and shifted to a southeastward subduction around the Eocene (~45 Ma) (Hall, 2002; Wu & Suppe, 2018) (Figure 1c). This southeastward subduction induced tectonic extension along the South China margin, causing several continental basement blocks to drift away from South China during the Eocene, ultimately leading to the seafloor spreading that formed the present-day SCS (Li et al., 2014, 2015; Mazur et al., 2012).

The oceanic basin is generally subdivided into three subbasins (SB): the northwestern (NWSB), southwestern (SWSB), and eastern (ESB) (Figure 1a). Integrated analyses of deep-tow magnetic anomaly data and cores from IODP Expedition 349 indicate that seafloor spreading in the NWSB initiated at ~33 Ma. The NWSB is recognized as the oldest sub-basin of the SCS (Briais et al., 1993; Barckhausen et al., 2014; Li et al., 2015; Johnson & Carlson, 1992), and notably its margin developed along remnant Mesozoic arcs (Li et al., 2018; Zhang et al., 2023; Zhao et al., 2019). Spreading ceased at ~15 Ma in the ESB and ~16 Ma in the SWSB (Li et al., 2014) as a consequence of the termination of PSCS subduction, which was marked by the collision of the Dangerous Grounds with Borneo during the middle Miocene (Holloway, 1982). With the closure of the PSCS, spreading transitioned from a magmatically dominated to a tectonically dominated regime in both NWSB (J. Z. Zhang et al., 2025) and ESB (Jiang et al., 2025). At present, remnants of the PSCS slab remain trapped in the asthenosphere beneath South China and Palawan (Fan et al., 2017; F. C. Li et al., 2018, 2020; Wu & Suppe, 2018).

During the spreading process, the ridge underwent two southward jumps at ~27 Ma and ~23 Ma (Ding et al., 2018) (Figure 1a). The latter event was further characterized by southwestward propagation of spreading (Barckhausen et al., 2014; Briais et al., 1993; Lee & Lawver, 1995; Li et al., 2014). The ridge jump and subsequent spreading at ~23.6 Ma (Li et al., 2014) may have been influenced by the Hainan mantle plume, as implied by geochemical and isotopic evidence for plume–ridge source mixing (Yu & Liu, 2020). Moreover, based on seismic profile interpretation, Z. Wang et al. (2025) suggest that the ridge jumps (~23.6) may also have been influenced by NW-directed far-field compressional stresses associated with extrusion driven by the India-Eurasia collision. The spreading rate reached its maximum during this period, averaging ~70 mm/yr (Li et al., 2014). Collectively, the southward ridge jumps and the progressive southwestward propagation shaped the highly asymmetric spreading pattern of the SCS basin, ultimately forming its characteristic V-shaped geometry (Le Pourhiet et al., 2018) (Figure 1a).

The prominent high magnetic anomaly zone along the northern margin of the SCS is interpreted as remnants of a Mesozoic Pacific subduction-related arc (Han et al., 2016; Li et al., 2018; P. Yan et al., 2014) (Figure 1a). By integrating reprocessed magnetic data with petrological evidence, Li et al. (2018) identified major magmatic bodies beneath the northern margin of the South China Sea, extending laterally ~60 km at depths of 18–24 km. Subsequent studies suggested that the northwestern margin of the SCS developed along a remnant magmatic arc, whereas the northeastern margin evolved along a remnant forearc basin (Figure 1a). These findings led to the inference that the remnants of the Mesozoic magmatic arc and forearc basin played a key role in controlling both the location and the style of SCS breakup (Li et al., 2018; Zhang et al., 2023; Zhao et al., 2019). This interpretation has been further corroborated by recent high-resolution seismic profiles (Xu et al., 2024) analog and numerical modeling results (G. X. Yang et al., 2025a).

Several major basement highs are distributed along the margins of the SWSB, including the Zhongsha Bank and Zhongjian Massif to the north, and the Reed Bank and Zhenghe Massif to the south (Figures 1a and 1b). The ocean–continent boundary (OCB) of the SWSB is markedly deflected and locally bends around these basement highs (Figures 1a and 1b). Geophysical observations combined with Pb isotopic data demonstrate that these basement highs are of continental origin and show affinity to the South China Block (Q. Yan et al., 2014). Wide-angle seismic profiles reveal that these blocks retain relatively thick crust, reaching ~13–20 km (Figure 1e), yet their ocean-facing margins underwent abrupt and rapid necking compared with the eastern margin (Figure 1d). Borehole data confirm a common Precambrian metamorphic basement beneath all four highs (Qiu et al., 2001; Sun et al., 2009; Yan & Liu, 2004; Ding et al., 2013). Consequently, during Cenozoic rifting and subsequent seafloor spreading, these basement highs likely acted as strong continental blocks that underwent limited thinning and deformation.

3 Analog modelling

3.1 Experimental setup and configurations

To investigate the role of differential subduction of the PSCS and the presence of crustal strength heterogeneities in shaping the V-shaped basins in general and the configuration of the SCS in particular, we designed a series of generic analog model experiments in which these factors were treated as variables (Figure 3).

In our experiments, a model base constructed by rigid PVC plates enclosing an elastic fabric (rubber belt) domain was employed to transmit extensional stress homogeneously across a central domain of variable shape (rectangular vs. trapezoid). It is noteworthy that stretching a basal rubber belt results in minor lateral contraction known as the Poisson effect giving rise to extension orthogonal shortening and slightly non-cylindrical structures (Zwaan et al. 2019, Liu et al., 2024). A similar effect of far-field compression parallel to the rift axis has been proposed for the case of the SCS (Le Pourhiet et al., 2018).

The apparatus was designed without lateral boundaries (Figure 2a). The orientation of the model in all visualizations in this paper mimics the geographic reference frame of the SCS in order to ease description and comparison (i.e. North-up). Two experimental series were conducted (Figure 3b). In Series U (“uniform extension” - U), the central elastic domain was rectangular with a uniform width of 30 cm along a length of 60 cm, bordered on both sides by 5-cm-wide rigid PVC base plates (Figure 2b). In Series D (“differential extension” - D), the elastic domain was trapezoid with a width decreasing linearly from 30 cm in the “west” of the model to 10 cm in the “east” (Figure 3b). Both series’ models were extended horizontally in “north-south” direction by a total of 10 cm at a constant rate of 0.01 mm/s using a motor-driven apparatus (Figure 3a). Under identical far-field stretching, Series U thus experienced a uniform extension of ~33%. In contrast, in Series D the extension had a spatial gradient: the western boundary of the fabric underwent ~33% extension, whereas the eastern boundary reached 100%, effectively simulating differential extension far from a rotation pole or associated as in our prototype with the eastward increase in subduction of the PSCS (F. C. Li et al., 2020).

Using the presence of strong blocks (B, representing basement highs in our prototype) and weak zone (W, representing a remnant magmatic arc in our prototype) as variables, each series consequently comprised four models: (1) a reference model (R) without strong blocks or weak zone (models UR and DR), (2) models with just strong blocks (UB and DB), (3) models with just weak zone (UW and DW), and (4) models incorporating both strong blocks and weak zone (UBW and DBW) (Figure 3b).

The selection of analogue materials and the thickness configuration of the upper and lower crust, as well as the remnant magmatic arc zone were determined following the approach of Yang et al. (2025a). Accordingly, the brittle upper crust was represented by a 1-cm thick layer of PVC powder exhibiting Mohr–Coulomb frictional behavior, with an internal friction angle of 34° and a cohesion of 36 Pa (Figure 3c). The ductile lower crust in the normal zone was modeled using a 0.75-cm thick layer of a PDMS1–corundum mixture (density 1150 kg/m^3, viscosity 7×10^4 Pa·s) (Figure 3c). A 4-cm-wide rectangular weak zone representing the ENE-trending remnant Mesozoic magmatic arc (Figure 3b, c) was placed in the lower crustal part of the model and simulated by a PDMS2–corundum–silicone oil mixture with a density of 1200 kg/m^3 and a viscosity of 10^4 Pa·s, i.e. 7 times weaker than the standard lower crust. The PDMS mixtures exhibited slightly non-Newtonian behavior with weak shear thinning.

Strong blocks were made of plasticine which exhibits strain-rate softening mimicking power-law creep in nature. Plasticine has relatively high viscosities ranging from ~10^5 to ~10^7 Pa·s (Zulauf & Zulauf, 2004; Koyi, 1997; Reber et al., 2020; Weijermars & Schmeling, 1986; Zulauf et al., 2011), i.e. about one order of magnitude higher than the standard lower crust. Stratigraphic and structural syntheses

(Franke et al., 2014), thermal-history constraints (Tang et al., 2014), and plate reconstructions (Clift et al., 2008) collectively suggest that, by the end of the Late Mesozoic, the basement highs of the southwestern sub-basin (SWSB) had already been isolated due to earlier rifting. Accordingly, in the initial configuration of our models, four pre-existing strong basement blocks along the continent–ocean boundary (COB) of the SWSB (Zhongjian Massif, Zhongsha Bank, Zhenghe Massif, and Reed Bank; Figure 1a, b) were represented by increasing the integrated crustal strength locally: Four cylindrical, high-viscosity plasticine bodies, each 3 cm in diameter (Figure 3b) were embedded within the weak silicone representing the standard ductile lower crust. Together with the overlying brittle material (Figure 3c) the integrated strength in the areas of the strong basement blocks is thus increased by about one order of magnitude (Table 1).

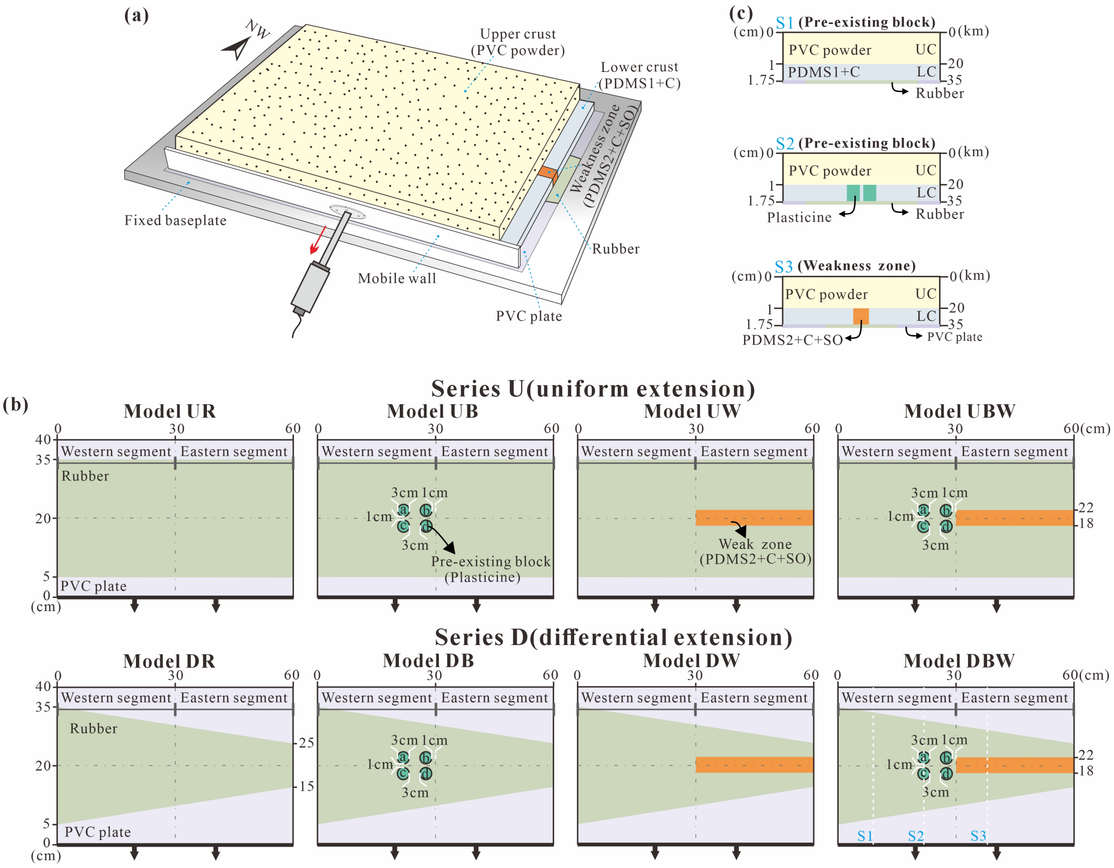

Figure 3. Model set-up. (a) Schematic of the experimental apparatus showing the initial condition. (b) Top view of experimental models under different initial configurations. Blocks a–d represent Zhongjian Massif, Zhongsha Bank (Macclesfield Bank), Zhenghe Massif, and Reed Bank (see Figure 1a), respectively. (c) Schematic cross sections illustrating the initial rheological layering of each segment. PDMS, Polydimethylsiloxane. C, corundum. SO, silicone oil.

Model evolution was documented by sequential top-view digital photography (Canon EOS 6D Mark II, 26.2 MP full-frame CMOS, 6240×4160 px, pixel size ≈5.76 µm, 14-bit RAW) taken at 1-minute intervals corresponding to 0.6 mm (or 2% with respect to the 30 cm wide elastic domain) of applied extension. These images were subsequently calibrated and analyzed using the image correlation technique Particle Image Velocimetry (PIV, Adam et al., 2005) to derive 2D surface velocity fields, differential displacement (Increment=1.2 mm), and cumulative areal strain using the software Tecplot 360 (Version 2024 R1). Additionally, a 3D scanner (ZEISS T-SCAN hawk 2, 0.5 mm point spacing) with stated volumetric accuracy (0.02 mm + 0.015 mm/m) was employed to scan the final topography of the model surface and, after the sand layer has been removed, of the model lower crust surfaces, providing digital elevation data of these two relevant surfaces. All experiments were conducted under constant laboratory conditions at a temperature of ~25 °C and relative humidity of ~50%.

3.2 Model scaling

The experiments were scaled to the natural prototype according to similarity criteria (Hubbert, 1937), ensuring geometric, kinematic, and dynamic similarity in the laboratory. Based on the adopted length ratio ($l_{m/n} = 5 \times 10^{-7}$, where m and n denote model and nature, respectively), 1 cm in the experiment corresponds to ~20 km in nature (Figure 3c). Consequently, the initial crustal thickness of ~35 km in the SCS region (Clift & Sun, 2006; Deng et al., 2020; Li et al., 2019) was scaled to 1.75 cm in the models (Figure 3c). Gravity inversion data indicate that the density at the top of the lower crust in the northern SCS is ~2870 kg/m³ (H. L. Li et al., 2020). This natural density (ρ_n) was represented in the models by a silicone–corundum mixture with $\rho_m \approx 1156$ kg/m³, corresponding to a density scaling factor of $\rho_{m/n} = 0.4$. The experiments were performed under normal gravity (9.8 m/s²), giving a gravity scale ratio of $g_{m/n} = 1$.

A stress ratio was then calculated as $\sigma_{m/n} = \rho_{m/n}\, g_{m/n}\, l_{m/n} = 2 \times 10^{-7}$. The stress ratio dictates the strength of the analogue materials used: For the brittle upper crust cohesion has to scale down accordingly by about six to seven orders of magnitude (from tens of MPa to Pa). For the viscously deforming ductile lower crust the properly scaled strength is derived by a combination of viscosity and strain rate: Model's standard lower crustal viscosity of 7.15×10^{4} Pa·s represents ~10^{22} Pa·s in nature lower crust (10^{21}–10^{23} Pa·s) (Clift et al., 2002; Zhang et al., 2001), resulting in a viscosity ratio $\eta_{m/n} = 7.15 \times 10^{-18}$. Combining the stress and viscosity ratios yields a strain-rate ratio (Weijermars & Schmeling, 1986) of $\varepsilon_{m/n} = \sigma_{m/n} / \eta_{m/n} = 2.8 \times 10^{10}$. The corresponding velocity ratio was calculated as $v_{m/n} = \varepsilon_{m/n}\, l_{m/n} = 1.4 \times 10^{4}$, such that the experimental reference velocity of 0.01 mm/s represents to ~2 cm/yr in nature ensuring kinematic and dynamic similarity.

The material properties and scaling parameters used in the experiments are summarized in Table 1.

Table 1 Model setup and material properties.

Layer	Rheology	Material	Thickness (m)		Density (kg/m^3)		Viscosity (Pa·s)	
			Model	Nature	Model	Nature	Model	Nature
Upper crust	Brittle	PVC (*C:* 36 Pa; μ: ~0.7)	$1\cdot10^{-2}$	$2\cdot10^{4}$	960	2400(1)	-	-
Standard lower crust	Viscous	PDMS1+C (1:0.3)	$7.5\cdot10^{-3}$	$1.5\cdot10^{4}$	1156	2870(2)	$7\cdot10^{4}$	$\sim10^{22}$
Weak lower crust (magmatic arc)	Low viscosity	PDMS2+C+SO (1:0.5:0.2)	$7.5\cdot10^{-3}$	$1.5\cdot10^{4}$	1200	-	$1\cdot10^{4}$	$\sim10^{21}$(3)
Strong lower crust (basement blocks)	High viscosity	Plasticine	$7.5\cdot10^{-3}$	$1.5\cdot10^{4}$	2000	-	$\sim10^{6}$(4)	$\sim10^{23}$

Note. (1) Liu et al., 2015; (2) H. L. Li et al., 2020; (3) Clift et al., 2002; (4) mean of plasticine's viscosity range in Zulauf and Zulauf, (2004). PDMS1, the density and viscosity are 913 kg/m^3 and $5.6\cdot10^{4}$ Pa·s, respectively; PDMS2, the density and viscosity are 898 kg/m^3, $1.75\cdot10^{4}$ Pa·s, respectively. PVC, plastic powder. PDMS, Polydimethylsiloxane. C, corundum. SO, silicone oil. *C* and μ denote cohesion and the friction coefficient, respectively.

3.3 Simplifications and Limitations

It is well established that brittle–ductile analogue experiments are constrained by the rheologies of the chosen materials and therefore cannot explicitly reproduce thermal processes such as geothermal gradients or thermally induced weakening of country rocks. Following earlier studies (Corti, 2008; McClay & White, 1995; Sokoutis & Willingshofer, 2011; Sun et al., 2000; Zwaan et al., 2019), we approximate these effects by prescribing an initially depth-dependent frictional strength controlled by pressure in the brittle upper crust and strain rate-dependent viscosity in the ductile lower crust.

Another limitation is the inability to reproduce magmatic processes and asthenospheric buoyancy. Consequently, melt-related phenomena such as magmatic underplating and the formation of new oceanic crust during seafloor spreading are not represented in our experiments. Independent observations, however, indicate that large-scale magmatism in the South China Sea mainly occurred after rifting and spreading (Cheng et al., 2021; Ding et al., 2018; Sun et al., 2019; Zhao et al., 2018, 2020). Therefore, our experiments, although restricted to mechanical forcing, can still effectively capture the first-order tectonic controls on rift evolution, including the locus of necking, fault kinematics, and strain partitioning.

Differential subduction of the PSCS is approximated by imposing an along-strike gradient in extension which would also be expected far from rotation poles. This gradient is achieved by varying the width of the elastic fabric. Under constant far-field stretching, fabrics of trapezoid shape generate a gradient in extension, effectively simulating the impact of differential subduction on the rift process in our prototype. The initial model setup (Figure 3c) assumes that the magmatic arc had not fully cooled before the breakup of the SCS and is thus weaker than the surrounding crust by about one order of magnitude. Our experiments primarily consider four major basement blocks distributed along the COB of the SWSB (Figure 1b). The stronger, pre-existing basement blocks that we assume are approximated as cylindrical bodies in the model, although in nature they are likely to be more irregular in shape. In the experiments, these cylinders are embedded within a weak ductile lower crust and overlain by a brittle upper crust (PVC powder), together approximating a colder and stronger crustal domain (strong blocks). This configuration is designed to capture the first-order integrated strength contrast between strong blocks and the surrounding lithosphere, rather than to reproduce the exact lithostratigraphic (geometric) position of the Precambrian metamorphic basement (Sun et al., 2009; Ding et al., 2013).

Despite these simplifications, consistent with prior analogue work (Corti et al., 2004; Molnar et al., 2017, 2020; Zwaan & Schreurs, 2023), we consider the present models appropriate for the specific scenario examined—namely, the pre–seafloor spreading stage during which differential PSCS subduction and inherited Mesozoic heterogeneities influenced V-shaped rift process in the SCS. However, because of the generic nature of the models, they may serve as models also for other rifts e.g. those far from rotation poles.

4 Experimental results

In this section, we first describe the effects of inherited strength heterogeneities, i.e. pre-existing strong basement blocks (B) and weak remnant magmatic arcs (W) under uniform extension (Series U). We then analyze the influence of these heterogeneities under differential extension driven by PSCS subduction (Series D). Finally, we provide a detailed analysis of the multi-factor experiment (Experiment DBW), focusing on geometric evolution, kinematic fields, and sectional characteristics. The evolutionary processes and kinematic fields of the other experiments are presented in Supplementary Figures S1–S7, with complete rift evolutions available in Supplementary Movies S1–S8.

4.1 Series U: Effects of inherited strength heterogeneities under uniform extension

Series U serves as the reference set, designed to simulate the influence of pre-existing strong and weak heterogeneities on the V-shaped opening of the South China Sea (SCS) under uniform extension, that is, without accounting for differential subduction of the PSCS. This series includes four experiments: UR, UB, UW, and UBW.

In the reference experiment UR without heterogeneities, extension was accommodated by a uniform conjugate fault pattern (Figure 4a). In Experiment UB, deformation localizes between the strong blocks (Figure 4b). Compared with Experiment UR, the presence of strong blocks disrupted the conjugate fault system, leading to the development of faults nearly perpendicular to the extension direction within block-bounded domains (Figure 4b). Areas around the blocks exhibit relatively high cumulative areal strain (Figures 4j and 4n). In Experiment UW, deformation localized within the weak zone (Figure 4c), where major faults formed perpendicular to the extension direction. In contrast, the western segment, similar to Experiment UR (Figures 4a, 4i, and 4m), exhibited a uniform conjugate fault patterns (Figure 4c) and lower cumulative areal strain localization (Figures 4k and 4o). Experiment UBW incorporated both strong blocks and weak zone, resulting in deformation patterns that combine features of Experiment UB in the western segment and Experiment UW in the eastern segment (Figures 4d and 4l). Compared with Experiment UW, deformation in Experiment UBW was more intensive along the weak zone, with several faults extending westward to link with those formed between the strong blocks (Figure 4d).

Under uniform extension, apart from localized deformation induced by strength heterogeneities, the eastern and western segments evolve almost synchronously along the rubber sheet (Figures S1–S4).

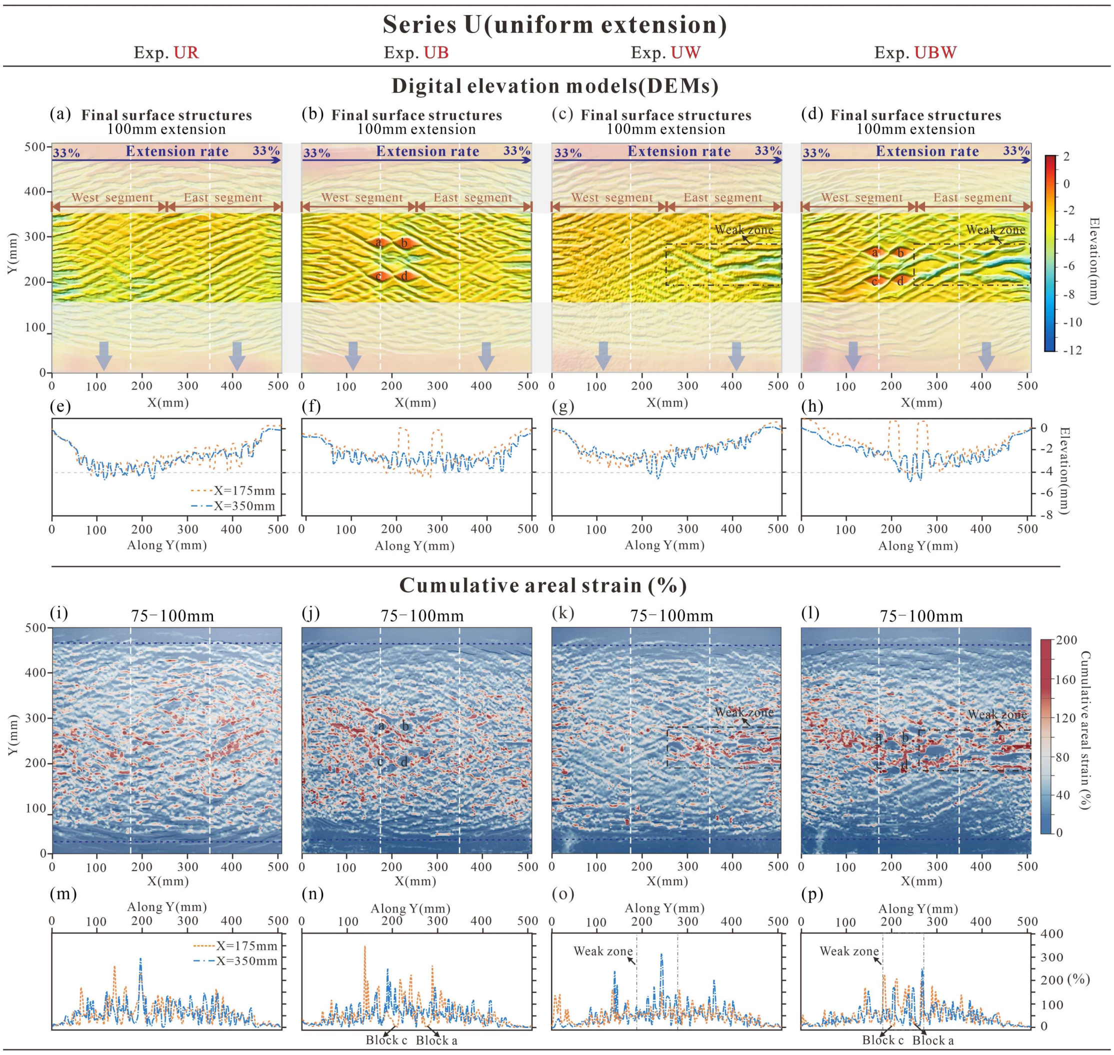

Figure 4. Digital elevation models (DEMs) and cumulative areal strain of final experimental results under uniform extensional configurations. Panels (a–d, i–l) show

3D DEMs of surface deformation (a–d) and cumulative areal strain (i–l). Panels (e–h, m–p) present 2D profile of DEM (e–h) and cumulative areal strain (m–p) along X = 175 (western segment) and X = 350 (eastern segment). Panels from left to right show the reference experiment, the experiment with only pre-existing strong blocks, the experiment with only a pre-existing weak zone, and the experiment incorporating both blocks and a weak zone. Purple arrows indicate the extension direction. White dashed lines mark the locations of profiles across strong blocks and the weak zone.

4.2 Series D: Effects of inherited heterogeneities under differential extension

Series D simulates the effects of differential extension resulting from differential subduction of the PSCS, as well as the influence of pre-existing heterogeneities. Complementary to Series U, it comprises four experiments: DR, DB, DW, and DBW.

In the reference Experiment DR (Figure 5a), only the effect of differential extension was considered. Accordingly, in the western segment, where the extension rate was relatively low and same as in series U, deformation resembled that in Experiment UR, being dominated by uniform pattern of conjugate faults (Figure 5a) and associated with relatively weak strain localization (Figures 5i and 5m). In contrast, the eastern segment, characterized by a 3 times higher extension rate, experienced earlier fault initiation (Figure S5a) and ultimately developed a denser fault network accompanied by uniform and intense thinning (Figure 5a) and higher strain localization (Figures 5i and 5m). Overall, deformation was diachronous, initiating in the east and progressively propagating westward (Figures S5a–S5d). The transition from west to east was gradual, and no evidence of localized deformation or the development of a V-shaped geometry was observed (Figure 5a).

In Experiment DB, strong blocks were introduced. Similar to Experiment DR (Figure 5a), the eastern segment experienced intense thinning under high extension (Figure 5b). In the western segment, faults around the strong blocks developed synchronously with those in the high-strain eastern domain during the early stages of extension (Figure S6). By the end of extension, intense deformation developed both in between the strong blocks and outside (Figure 5b). Cumulative areal strain between the blocks exceeds that of the strongly extended eastern segment (Figure 5f); accordingly, thinning between the blocks is also greater (Figure 5n). Deformation in Experiment DW localized along the weak zone in the eastern segment from the early stage on (Figure S7a). During subsequent extension, deformation in weak zone showed a westward propagation, although the propagation distance was very limited

(Figures 5c and S7). In contrast, deformation in the western segment resembled that in Experiment DR, being more diffuse and weaker than in the eastern segment (Figure 5c). Cumulative areal strain is significantly higher in the east than in the west (Figures 5k and 5o).

Experiment DBW incorporated both strong blocks and weak zone (Figure 5d). The main deformation zone developed along the weak zone in the eastern segment and connected with the zone of intense deformation between the strong blocks in the western segment (Figure 5d). Because the deformation zone between the strong blocks was relatively narrow, the geometry of the main deformation zone exhibited a westward contraction and terminated between the two westernmost blocks. The minimum DEM elevation between the strong blocks in Experiment DBW was slightly higher than that within the weak zone (Figure 5h). The evolutionary process and thinning feature of this multi-factor-controlled experiment is described in detail in Section 4.3.

Overall, deformation in Series U (Figures 4a–4d) was generally weaker than in Series D (Figures 5a–5d). This difference arises from the higher extension rate in Series D (33–100%) compared with the uniform 33% extension applied in Series U.

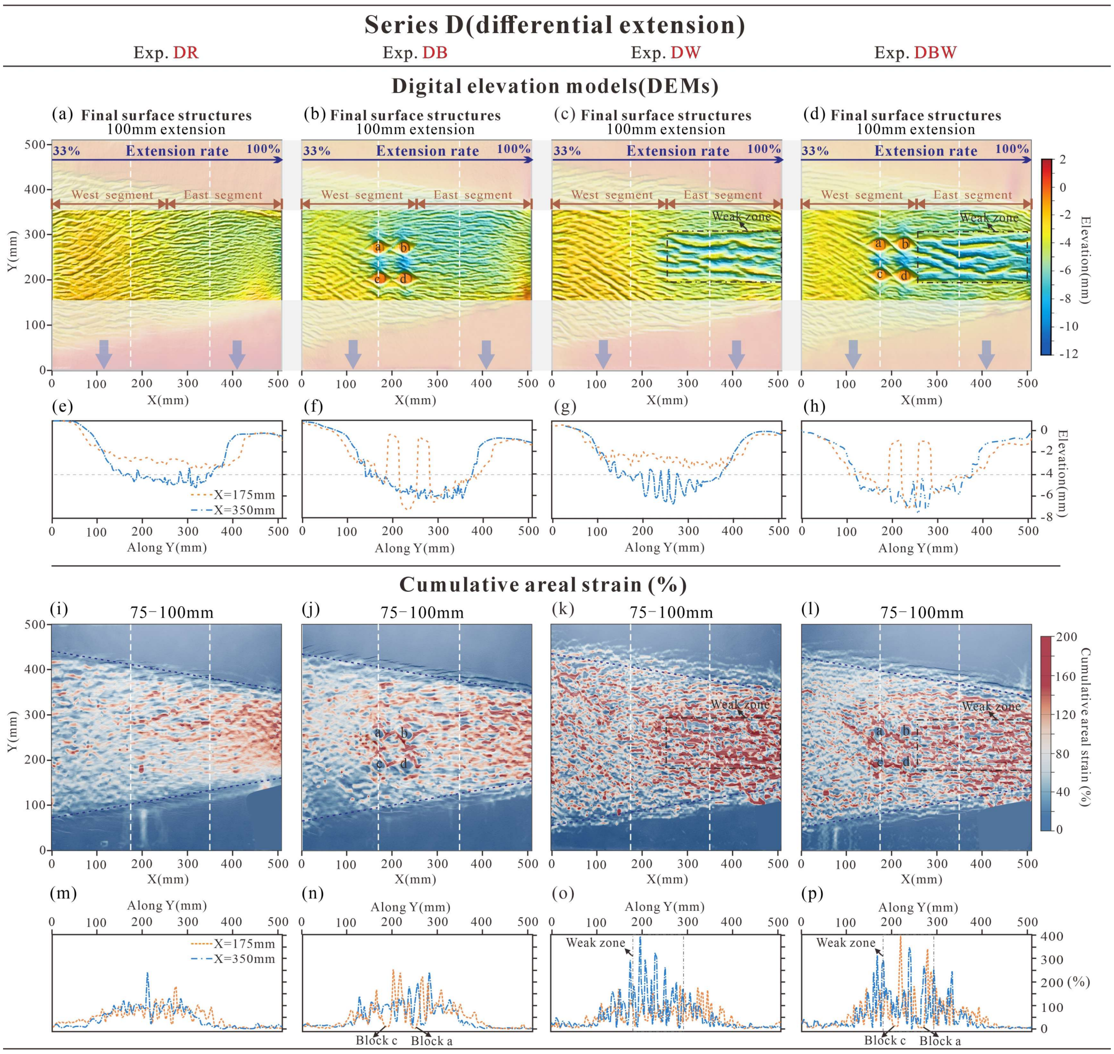

Figure 5. Digital elevation models (DEMs) and cumulative areal strain of final experimental results under different extensional configurations. Panels (a–d, i–l) show 3D DEMs of surface deformation (a–d) and cumulative areal strain (i–l). Panels (e–h, m–p) present 2D profile of DEM (e–h) and cumulative areal strain (m–p) along X = 175 (western segment) and X = 350 (eastern segment). Panels from left to right show the reference experiment, the experiment with only pre-existing strong blocks, the experiment with only a pre-existing weak zone, and the experiment incorporating both blocks and a weak zone. Purple arrows indicate the extension direction. White dashed lines mark the locations of profiles across strong blocks and the weak zone. Beyond the elastic fabric (rubber belt), local deformation (uplift) of the plastic plates induced by tilting during extension has been visually masked using a uniform color to avoid misinterpretation. The original cumulative areal strain figures are shown in Figures S5–S7, and the original DEM datasets are available via data sharing (repository).

4.3 Detailed analysis of geometric and kinematic features of the multi-factor experiment (Experiment DBW)

Figure 6 illustrates the evolutionary process of Experiment DBW, together with the corresponding differential displacement, cumulative areal strain, and shear strain. For clarity, we refer to the region with strong blocks as the “block zone”, the eastern segment corresponding to a remnant magmatic arc as the “weak zone”, and the homogeneous region without heterogeneities as the “normal zone” (Figure 3b).

At the early extension stage (25 mm extension; Figure 5a), deformation was mainly concentrated within the weak zone in eastern segment. In the western block zone, faults developed along the boundaries of the strong blocks, accompanied by minor subsidence between them, but fault offsets were limited (Figure 6a). At 50 mm of extension (Figure 6b), strain remained concentrated within the weak zone in eastern segment. Narrow depressions bounded by small-offset faults formed between strong blocks in the western segment, with cumulative strain markedly higher (Figure 6j) than during the early stage (Figure 6i). Shear strain around strong blocks a and c also intensified (Figure 6n). In addition to the major faults within the weak zone, several secondary faults developed along both its northern and southern flanks (Figure 6b). Deformation along the outsides of the main deformation zone progressively decreases from east to west (Figures 6b and 6j). The westernmost normal zone remained unfaulted and accommodated extension mainly through crustal thinning during this stage (Figure 6b).

With further extension to 75 mm (Figure 6c), faulting in the main deformation zone was dominated by the continued growth and linkage of faults developed at previous stage, while deformation widened both within the weak zone and between strong blocks (Figures 6c and 6k). The early-formed grabens between strong blocks did not propagate farther west (Figure 6c and 6k). On the northern and southern flanks of the main deformation zone, zones of high cumulative strain expanded westward (Figure 6k) compared with the previous stage (Figure 6j), accompanied by the development of westward-propagating faults (Figure 6c). In the normal zone at the westernmost margin, a set of minor faults also formed (Figure 6c), although cumulative areal strain there remained much lower than in the block and weak zone (Figure 6k).

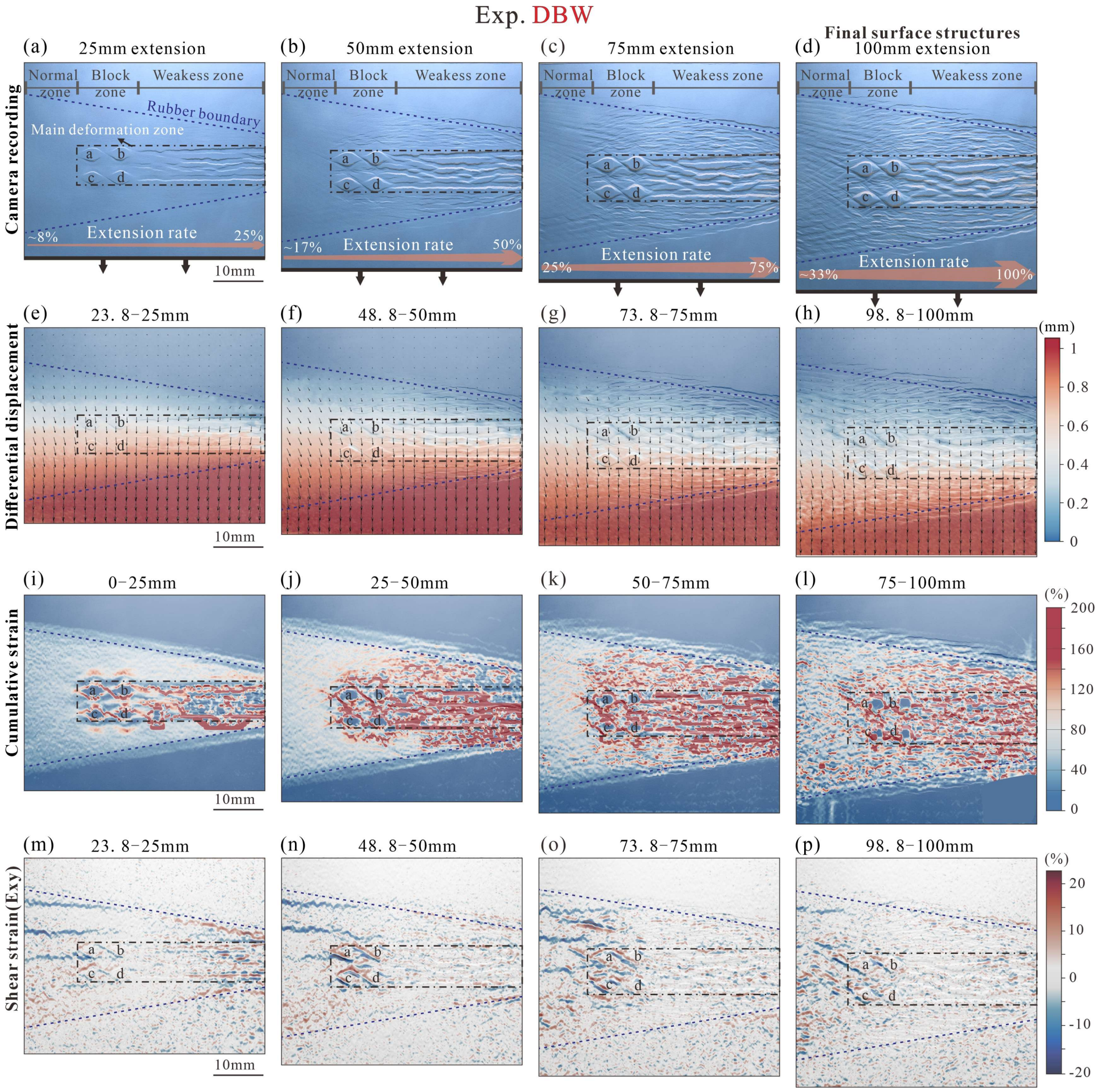

Figure 6. Evolution and particle image velocimetry (PIV) analysis of the multi-factor Experiment DBW. (a–d) Top-view figures showing the evolutionary stages. (e–h) Differential displacement fields and associated displacement directions. (i–l) Cumulative strain field maps. (m–p) Shear strain field maps.

In the final stage (Figure 6d), most faults continued their growth, with only a limited number of new faults nucleating in the normal zone. Strain between strong blocks (Figure 6h) is comparable to that in the weak zone (Figure 6l), indicating that both experienced similarly localized deformation at this stage. Thinning between strong blocks approached the magnitude observed within the weak zone (Figure 5h). Ultimately, deformation within the weak zone broadened and deepened, whereas in the western segment it remained confined to narrow block-bounded domains and did not propagate farther west. As a result, the main deformation zone evolved into a geometry that was wide in the east (weak zone) and narrow in the west (block zone), while deformation in the normal zone persisted as diffuse and gentle (Figure 6d). Collectively, these features gave the overall deformation zone a distinct V-shaped configuration (Figure 5d).

Throughout the evolution, most strong blocks were surrounded not only by localized extension but also high shear strains (Figures 6m–6p), while shear strain along the eastern margins of the blocks b and d adjacent to the weak zone was relatively weak (Figures 6m–6p).

By combining the DEMs of the upper and lower crust (Figure 7) in Experiment DBW, the thinning characteristics of both layers under the influence of multi-factors can be quantitatively illustrated. Accordingly, the lower-crustal surface also shows pronounced thinning both within the weak zone and between strong blocks. Moreover, significant localized thinning occurred on the outer side of blocks, forming arcuate depressions (Figure 7b). This pattern is likely caused by compositional heterogeneity between the strong blocks and the surrounding standard lower crust. Deformation in the lower crust within the weak zone and between strong blocks (a–c and b–d) appears spatially isolated (Figure 7b), whereas brittle deformation in the upper crust was laterally interconnected and continuous due to fault propagation (Figure 7a).

To further assess crustal thinning across different domains, we extracted three paired profiles of the upper and lower crustal surfaces. These profiles cross the normal zone (L1 and L1′), strong block zone (L2 and L2′), and the weak zone (L3 and L3′) at corresponding positions (Figures 7a and 7b). In the normal zone, both the upper and lower crust experienced relatively gentle thinning (Figures 7c, 7d, and 7e). Across the blocks, the upper and lower crust topography reveal a strong spatial coupling of thinning within the main deformation zone (Figure 7f). Strong thinning occurred between strong blocks in both the upper and lower crust, where thickness decreased abruptly, forming a narrow rift zone (Figure 7f). The strong blocks behaved as quasi-rigid domains during extension, undergoing little thinning, and their thickness remained significantly greater than that of the surrounding lower crust (Figure 7f). Correspondingly, the upper crust above the strong blocks also appeared to undergo little thinning. In the line across the weak zone (L3 and L3′; Figure 7g), the upper crust experienced more thinning than that in either the block-bounded domains or the normal zone (Figure 7c). By contrast, thinning in the lower crust was slightly greater than in the normal zone but considerably less than that between strong blocks (Figure 7d).

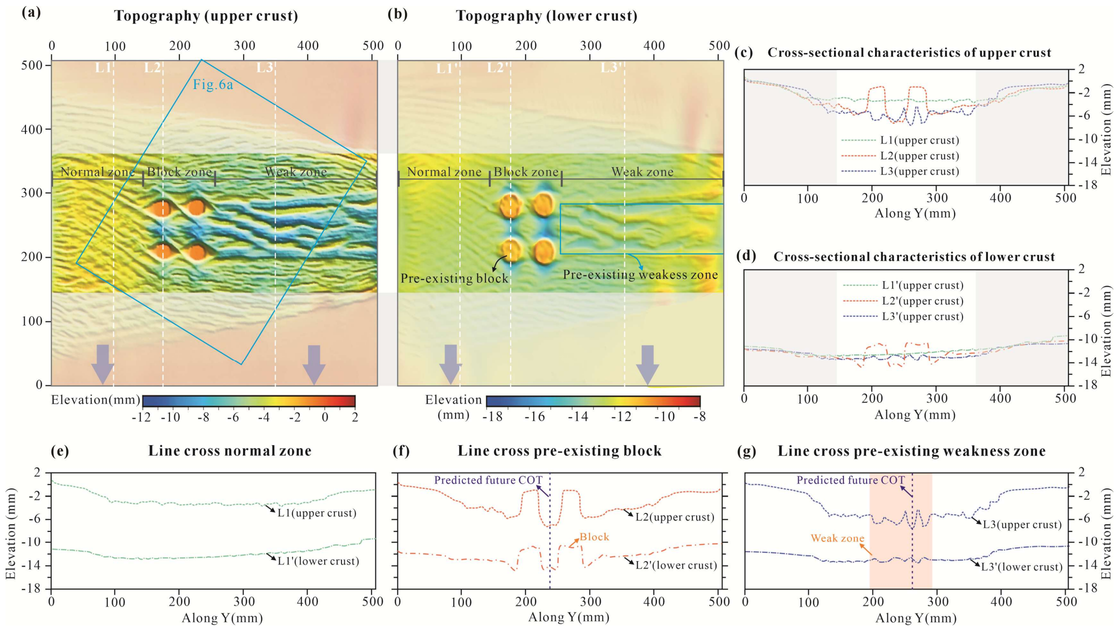

Figure 7. Digital elevation models (DEMs) of the upper and lower crust in Experiment DBW. (a, b) DEMs of the upper and lower crustal surfaces. (c, d) Comparison of thinning characteristics in different domains of the upper and lower crust. (e-g) 2D DEM profiles across the normal zone, block zone, and weak zone. The locations of the 2D DEM profiles are indicated in panels (a) and (b).

5 Discussion

5.1. Hierarchy of controlling factors

A comparative analysis of the evolutionary processes and final structural characteristics of all experiments clarifies the hierarchy and interactions among the three factors considered in this study (differential extension rate, pre-existing strong blocks, and pre-existing magmatic arc) in shaping the V-shaped rifting of the SCS.

Under uniform extension (Series U), the reference model (Experiment UR) exhibited evenly distributed, synchronous conjugate faults along the rift axis, resulting in relatively uniform crustal thinning across both the western and eastern segments (Figures 4a, 4e and S1). In this context, deformation in all experiments remained relatively gentle (Figures 4a–4d), with strong blocks and weak zone influencing only the spatial localization of deformation, without producing significant along-axis strain transfer (Figures S2–S4). In contrast, under differential extension (Series D), the reference model (Experiment DR) shows that faults in the eastern segment, where extension rates were higher, initiated earlier and progressively propagated westward, producing diachronous deformation (Figure S5). By the end of extension, the eastern domain experienced much stronger thinning, whereas crustal thickness gradually increased westward (Figures 5a and 5e). Although a few faults developed around strong blocks at an early stage in western segment, overall deformation remained dominated by the diachronous pattern of east-to-west propagation (Figures 6 and S6–S7).

Consistent with previous studies (Brune & Autin, 2013; Corti et al., 2007; Ding & Li, 2016; Heron et al., 2016; Sun et al., 2009; Zwaan et al., 2019, 2021, 2022), strain preferentially localized along strong block boundaries (Experiment UB, Figure S2i; Experiment DB, Figure S6i) and within the weak zone (Experiment UW, Figure S3i; Experiment DW, Figure S7i), regardless of extension mode. However, the final outcomes differ significantly between Series U and Series D. In Series U, localized deformation remained moderate and spatially limited because of the relatively low overall extension rate (~33%) (Figures 4b–4d). In contrast, in Series D, the influence of strength heterogeneities became much more pronounced, reflecting the amplifying effect of higher extension rates.

Experiments with only strong blocks (Experiment UB and Experiment DB) show that strain localized between blocks in the western segment, producing a narrow rift zone (Experiment UB, Figure 4b; Experiment DB, Figure 5b). Under uniform extension, deformation outside this narrow zone remained relatively homogeneous. In Experiment DB, where the extension rate was higher, deformation between strong blocks intensified, generating narrow and deep rifts that even exceeded the strong thinning observed in the eastern domain (Figures 5b and 5f). Faulting thus transitioned from a dense network in the eastern segment to fewer but more intense faults between strong blocks in the western segment (Figure 5b). The presence of strong blocks not only intensified deformation between them but also modified the overall rift geometry by imparting wavy margins along block boundaries and generating associated troughs on their flanks (Figure 5b).

Weak zone controlled the location of deformation in the eastern segment. Under uniform extension (Experiment UW), deformation within the weak zone was relatively limited in both extent and intensity, and oblique conjugate faults developed along its western part under the influence of the adjacent normal zone (Figure 4c). In contrast, under differential extension (Experiment DW), deformation within the weak zone intensified markedly, and the transition from the eastern segment into the adjacent normal zone was accommodated by a greater number of faults (Figure 5c).

Comparison of the multi-factor experiments (Experiment UBW and Experiment

DBW) with those involving only a weak zone (Experiment UW and Experiment DW) reveals that the presence of strong blocks not only concentrated strain within block-bounded domains in the western segment but also facilitated deformation within the adjacent eastern weak zone, allowing faults to propagate westward and link across the two domains. Under uniform extension (Experiment UBW), unlike the localized deformation observed in Experiment UW (Figure 4c), several faults propagated from the weak zone into the block-bounded domains and eventually connected with main faults between the strong blocks (Figure 4d). Under differential extension (Experiment DBW), in contrast to the fault-number adjustments seen in Experiment DW (Figure 5c), deformation localized at block boundaries, generating a markedly narrower deformation zone between blocks (Figure 5d). This zone ultimately merged with the wide and deep deformation zone in the eastern segment, forming a V-shaped rift that was wide in the east and narrow in the west (Figure 5d). Moreover, deformation under differential extension exhibited a diachronous pattern, initiating earlier in the east and progressively propagating westward (Figures 6a–6d).

The differing degrees of control exerted by strength heterogeneities under uniform and differential extension demonstrate that the progressive increase in extension rate from west to east not only produced diachronous thinning but also amplified strain within strong block- and weakness-controlled domains, which were already preferential loci of deformation under uniform extension (Figures S1–S4). As a result, the eastern domain was dominated by intense deformation along the weak zone, whereas in the west strain was mainly localized between strong blocks, leading to a westward narrowing rift (Figure 5c).

In summary, among the three factors considered, differential extension represents the first-order tectonic control on rift evolution. The progressive westward decrease in extension rate governed strain magnitude, the diachronous activity of faults, and the differential thinning of the crust, while also modulating the expression of inherited structures. In contrast, strength heterogeneities acted as second-order tectonic factors. Weak zone focused strain and guided the geometry of rift boundaries, leading to early, wide, and intense thinning. Strong blocks localized strain within narrow domains and defined irregular rift margins, producing the characteristic opening angle of the V-shaped rift. Together, these three factors form a hierarchical control system: the first-order factor differential extension determined the overall framework and timing of rifting, whereas the second-order factors — the strong blocks and weak zone —

refined and segmented the geometry of the respective domains. These findings are consistent with previous geodynamic studies that emphasize the importance of initial rheological structure and extension rate in governing the architecture of early rift basins (Brun, 2002; Huismans & Beaumont, 2002, 2014; Pérez-Gussinyé et al., 2006; Tetreault & Buiter, 2018).

5.2 Comparison with observations from the South China Sea

In this section, by comparing the results of the multi-factor experiment (Experiment DBW) with natural observations from the SCS in both map view and cross-section, we aim to further elucidate the geodynamic processes and mechanisms that governed its V-shaped opening.

The experiment DBW reveals that in the early stages of extension, the eastern segment, subjected to higher extension rates, experienced strong strain localization within the weak zone, resulting in greater deformation and a denser fault network. By comparison, the western segment developed only scattered faults around strong block margins (Figure 6a). With progressive stretching, deformation propagated westward (Figure 6d), producing diachronous rifting. This finding is consistent with the east–west diachronism observed in the northern margin of the SCS, where initial faulting in the Pearl River Mouth Basin (Figure 1a; northeast margin) preceded that in the Qiongdongnan Basin (Figure 1a; northwest margin) (Shi et al., 2011; Wang et al., 2021). Further evidence supporting this diachronism comes from the T70 unconformity (~33 Ma, Eocene), which marks the onset of seafloor spreading in the SCS: prior to this unconformity, both the average faulting rate and the average sediment thickness were higher in the Pearl River Mouth Basin than in the adjacent Qiongdongnan Basin (Xia et al., 2016).

Experiment DBW reproduces a V-shaped geometry consistent with that of the South China Sea. In the eastern segment, where extension rates were higher, deformation was strongly localized along the weak zone, forming a wide and deep deformation belt (Figures 5d, 5h, and 8a). This finding corroborates earlier interpretations that the eastern weak zone controlled the locus of breakup (P. Yan et al., 2014; Han et al., 2016; Li et al., 2018; G. X. Yang et al., 2025a). In contrast, in the western segment, material heterogeneity associated with continental basement blocks promoted localized strain concentration, producing narrow and deep rift zones between blocks (Figures 5d, 5h, and 8a), which may be regarded as precursors to seafloor spreading in the SWSB. Collectively, these processes formed an east-wide, west-narrow V-shaped rift geometry, closely resembling the present-day configuration of the SCS basin (Figure 8b).

Experiment DBW further demonstrates that strength heterogeneity promoted the formation of depressions around strong blocks (Figure 8a). These experimental features correspond to natural troughs such as the Xisha (W. Wang et al., 2025) and Zhongsha (Li et al., 2021) troughs (Figure 8b). Previous numerical (Qing et al., 2024) and analog models (Sun et al., 2009) similarly demonstrate that strong blocks enhance strain localization in the adjacent crust, leading to the development of deep troughs. In addition, several faults developed oblique to the main rift trend around strong blocks in the experiments (Figure 8a), resembling the oblique faults observed around major continental basement blocks (e.g., Zhongsha Bank, Zhongjian Massif, Reed Bank, Zhenghe Massif) on the northern and southern margins of the SWSB (Figures 1b and 8b). Cumulative strain results further indicate that these oblique faults developed relatively early and contained shear components (Figure 6m). However, the shear strain of oblique faults adjacent to the weak zone remained relatively low (Figures 6m–6p).

In addition to the plan-view geometry, the deformation style in experiment DBW is also consistent well with natural observations. In the eastern segment of our experiment, the weak zone representing a remnant Mesozoic magmatic arc produced intense crustal thinning, but with decoupled behavior between the brittle upper and ductile lower crust (Figure 7g). The upper crust was strongly thinned relative to the block and normal zones (Figures 7a and 7c), whereas the lower crust remained relatively flat, with weaker thinning than that in block-bounded zone (Figures 7b and 7d). This difference may be attributed to ductile flow within the weak lower crust representing the remnant magmatic arc. Such decoupling is also observed along the northern margin of the SCS. High-resolution seismic profiles across the Kaiping Rift, located within the remnant magmatic arc zone (Figure 1a), reveal a sub-horizontal Moho and exhumed ductile lower crust beneath an extremely thinned brittle crust (Xu et al., 2024).

Seismic profiles across the western margin reveal relatively thick basement blocks, whereas their margins underwent sharp necking (Figure 1e) and localized detachments that remained active from the Late Cretaceous to the Paleogene (Ding et al., 2012; Ding & Li, 2016; Pichot et al., 2014; Qiu et al., 2011; Savva et al., 2014). Numerical modeling and seismic observations (Cameselle et al., 2020) further indicate that necking between strong blocks reached a stage high enough for the lower crust to deform in a brittle manner, consistent with sequential faulting models of magma-poor rifted margins (Ranero & Pérez-Gussinyé, 2010). In our analogue experiments, similar to the behavior of strong basement blocks in the SCS, both the upper and lower crust underwent only minor thinning overall, with strain concentrated between adjacent blocks. This promoted strongly coupled thinning of the upper and lower crust, with the lower crust exhibiting markedly stronger thinning than that observed in the eastern weak zone (Figure 7d). This process produced narrow necking domains, closely corresponding to seismic evidence of block-bounded structures previously reported.

Experiment DBW finally showed that the westernmost normal zone accommodated extension through distributed deformation, with relatively uniform thinning of both upper and lower crust (Figures 7a, 7b, and 7e). This thinning was weaker than in strong block- or weak zone-controlled domains (Figures 7c and 7d). Similar patterns are observed near the southwestern tip of seafloor spreading, where crust thins diffusely without strong localization (Wei et al., 2020; C. L. Zhang et al., 2025). However, because continental extension persisted in this region even after seafloor spreading initiated elsewhere in the SCS (Hayes & Nissen, 2005; Franke et al., 2014; Pichot et al., 2014; Savva et al., 2014), this domain ultimately experienced more prolonged extension and greater crustal thinning, with average Moho depths reaching ~16 km (Cameselle et al., 2017).

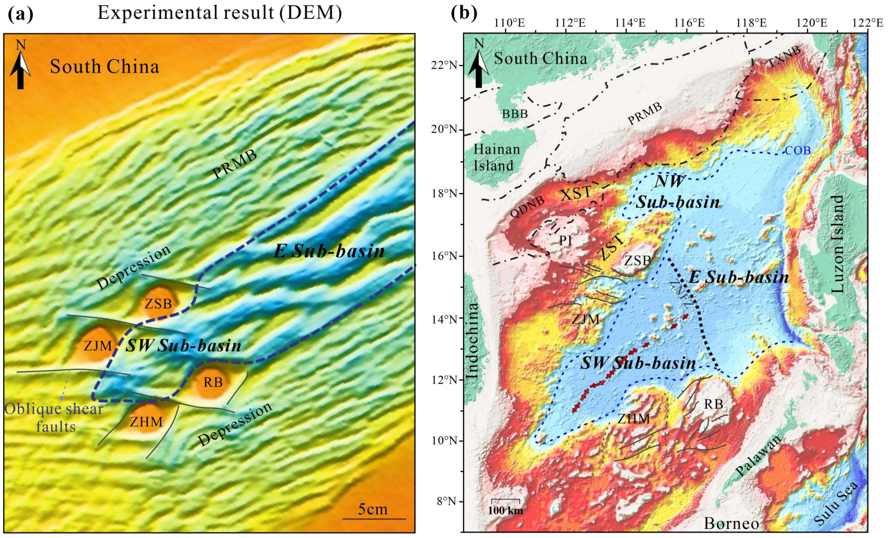

Figure 8. Comparison between the final DEM of the multi-factor Experiment DBW and natural observations from the South China Sea. Faults around natural basement blocks are modified after Ding & Li (2016). QDNB, Qiongdongnan Basin; PRMB,

Pearl River Mouth Basin; XST, Xisha Trough; ZNFZ, Zhongnan Fracture Zone; COB, Continent–ocean boundary; ZST, Zhongsha Trough; ZJM, Zhongjian Massif; ZSB, Zhongsha Bank (Macclesfield Bank); ZHM, Zhenghe Massif; RB, Reed Bank; PI, Paracel Islands (Xisha Islands).

Overall, the spatiotemporal evolution and structural features of Experiment DBW, which integrates differential extension, pre-existing strong blocks, and weak zone, show strong correspondence with natural observations from the SCS. These include the east–west diachronism of early rifting, the V-shaped basin geometry, block-related structural patterns, and contrasting crustal thinning styles. When combined with the factor hierarchy established in Section 5.1, the results indicate that differential extension constituted the primary geodynamic control on the timing of rift initiation, whereas strong blocks and weak zone served as secondary structural factors that determined the loci of deformation and the configuration of rift boundaries. The experiments therefore suggest that the V-shaped opening of the SCS was not the product of a single mechanism but rather the integrated outcome of interactions between differential extension and inherited lithospheric heterogeneities.

5.3 Implications for the deformation process of the SCS

Based on the experimental results and previous studies on the tectonic evolution of the SCS (Ding & Li, 2016; Hall, 2002; F. C. Li et al., 2018, 2020; Sun et al., 2009, 2019; Wu & Suppe, 2018), the formation process of the SCS can be broadly divided into four stages.

Stage 1: Pre-rift stage (before ~65 Ma)

The Late Cretaceous was a critical period for the evolution of the SCS. A series of Cretaceous faults and magmatic intrusions developed along the northern margin of the SCS in response to paleo-Pacific subduction to the northwest (Zhou et al., 2005; Ye et al., 2018, 2020) (Figure 9a). Continuous magmatism driven by corner flow, related to northwestward subduction of the PSCS, may have further weakened the lithosphere of the region (Hall, 2002; F. C. Li et al., 2020; Wu & Suppe, 2018). Consequently, the magmatic arcs formed during this stage are interpreted as weak zone that strongly influenced the later breakup of the SCS (Li et al., 2018; G. X. Yang et al., 2025a; Zhang et al., 2023; Zhao et al., 2019). Meanwhile, in the western domain, basement blocks had already drifted away from the South China margin and became separated due to early rifting and spreading processes associated with the retreat of the paleo-Pacific plate (Figure 9a) (Clift et al., 2008; Hall, 2012; Franke et al., 2014; Tang et al., 2014; Ding & Li, 2016).

Stage 2: Rift stage (~45–33Ma)

Following Late Mesozoic magmatism in southern China, the subduction direction of the PSCS switched polarity towards during the Eocene (~45 Ma). From now on the PSCS subducted southeastward beneath Borneo with eastward increasing rate producing a scissor-like subduction geometry (Figures 1c and 9b) (Hall, 2002; Hutchison, 2004; Wu & Suppe, 2018). Our experiments demonstrate that the resulting differential extension rates may have played a key role in early rifting of the SCS. Under higher extension rates, the eastern remnant arc weak zone experienced earlier and more intense thinning, producing a wide and deep rift (Figures 5a, 6 and 9b). In contrast, deformation in the west initially localized around strong basement blocks (Figure 6a) and progressively developed into narrow, deep rifts between blocks (Figures 5d and 6d). Collectively, these processes formed a westward narrowing V-shaped rift geometry (Figures 5d and 9b). In addition, a series of shear-related faults and troughs developed around the basement blocks (Figure 9b).

Stage 3: Initiation of seafloor spreading in eastern segment (~33–23 Ma)

With continued differential southeastward subduction of the PSCS beneath Borneo (Clift et al., 2008; Cullen et al., 2010; Hall, 2002), seafloor spreading initiated in the northwestern sub-basin (NWSB, eastern segment) at ~33 Ma (Li et al., 2014) (Figure 9c). The NWSB margin developed along remnant Mesozoic arcs (Li et al., 2018; Zhang et al., 2023; Zhao et al., 2019). This observation, combined with our experimental results, suggests that inherited volcanic arc crust acted as a weak zone that, together with the larger extension rate driven by differential PSCS subduction, facilitated the onset of spreading in the east (Figure 9c). In addition, syn-tectonic magmatism likely contributed to breakup: IODP Expeditions 367/368 on the northern SCS distal margin and subsequent interpretations (Ding et al., 2020) suggest a short-lived magmatic event during the latest stage of rifting that intruded the edge of the thinned continental crust, triggering continental breakup and the onset of steady-state seafloor spreading.

Stage 4: Spreading propagation and termination (~23–16Ma)

At ~23 Ma, a ridge jump occurred in the eastern sub-basin (ESB), after which spreading propagated southwestward and led to the formation of the southwestern sub-basin (SWSB, Barckhausen and Roeser, 2004; Barckhausen et al., 2014; Briais et al., 1993; Cullen et al., 2010; Franke et al., 2014; Li et al., 2014). Based on our experimental results, the initial spreading was likely confined to a narrow necking zone of relative weakness between stronger basement massifs. Subsequently, under limited extension associated with the differential subduction of the PSCS and the focusing effect of strong blocks, a restricted spreading center developed, which, together with the ESB, ultimately produced a V-shaped oceanic basin (Figures 1c and 9d). Spreading ceased at ~16 Ma (Li et al., 2014), likely associated with the termination of PSCS subduction.

Our experiments demonstrated that the V-shaped configuration of the rifting and spreading reflects a structural-rheologic inheritance: a V-shaped rift system already formed prior to seafloor spreading due to the combined effects of differential extension and inherited strength heterogeneities. The eastern domain, controlled by both remnant Mesozoic arc weakness and higher extension rates, underwent stronger pre-spreading rifting and thus initiated spreading earlier. In contrast, the western domain, influenced by pre-existing basement blocks and lower extension rates, developed localized strain between blocks, shaping the western narrowing of the early SCS. Later seafloor spreading propagated southwestward along this inherited V-shaped rift.

Apart from the factors considered in this study, additional processes may also have contributed to ridge jumps and rift propagation in the SCS, including far-field stresses from the west-to-east topographic gradient across the Indochinese Peninsula imposing a basin axis-normal compression (Le Pourhiet et al., 2018), the Hainan mantle plume (Yu & Liu, 2020), and NW-directed far-field compressional stresses associated with extrusion driven by the India–Eurasia collision (Z. Wang et al., 2025). In addition, thermo-mechanical numerical simulations reveal that syn-rift margin architecture may also have been influenced by surficial loads (H. B. Yang et al., 2025). However, fully resolving these dynamics, particularly during the spreading stage, requires 3D thermo-mechanical modeling that explicitly incorporates the combined effects of far-field stress, inherited strength heterogeneities, plume–ridge interactions, and surficial load influences.

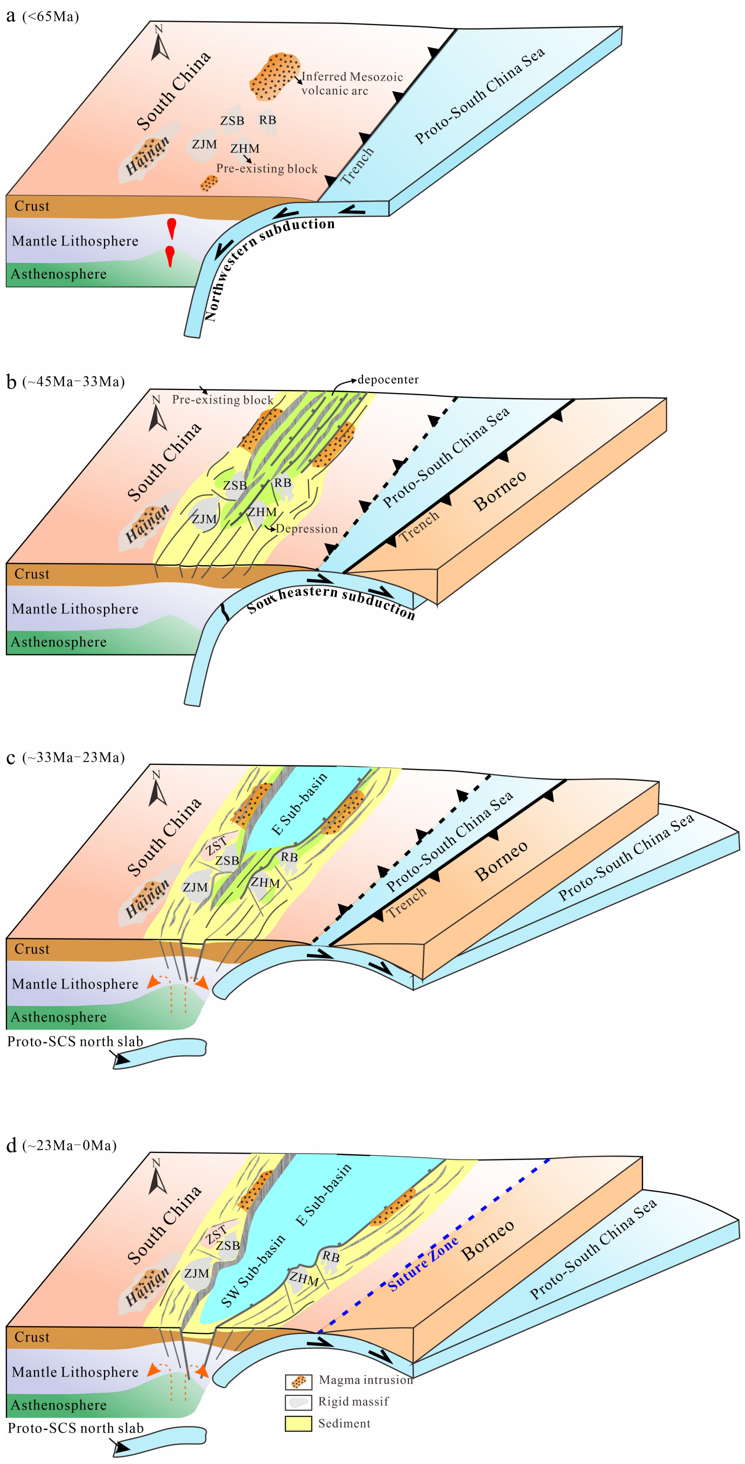

Figure 9. Schematic illustration of the four-stage evolution of the South China Sea from initial rifting to seafloor spreading. (a) Pre-rift stage. (b) Rift stage. (c) Initiation of seafloor spreading in the eastern segment. (d) Subsequent spreading propagation and termination. The schematic representation of subduction polarity reversal, slab tearing, and stagnation is modified after F. C. Li et al. (2020). ZST, Zhongsha Trough; ZJM, Zhongjian Massif; ZSB, Zhongsha Bank (Macclesfield Bank); ZHM, Zhenghe Massif; RB, Reed Bank.

6 Conclusion

Our experimental results demonstrate how propagating, V-shaped continental to oceanic rift basins can develop far from plate tectonic rotation poles governed by the combined effects of differential extension and inherited strength heterogeneities. Applied to the South China Sea, our experimental resultssuggest that differential extension, driven by differential subduction of the PSCS southeastward beneath Borneo with eastward increasing rate, was the primary geodynamic factor controlling the timing and magnitude of rifting, producing east–west diachronism in faulting and crustal thinning. Remnant Mesozoic arcs and pre-existing continental basement blocks acted as secondary structural-rheologic factors, localizing strain and modifying the basin geometry and deformation pattern. Under their combined influence, the eastern segment developed a wide and deep rift along the remnant magmatic arc under high extension rates, whereas the western segment localized strain between basement blocks to form narrow, deep rift zones. Together, these processes produced the characteristic westward narrowing V-shaped rift preceding seafloor spreading in the SCS.

By integrating our experimental results with regional geological and geophysical observations, we propose a four-stage evolutionary model for the SCS, encompassing the pre-rift stage, rift stage, initiation of seafloor spreading in the eastern segment, and subsequent spreading propagation and termination. This framework highlights a spatial inheritance between rifting and spreading: the V-shaped geometry was initially established by inherited Mesozoic structures and differential extension, while seafloor spreading likely began in the eastern sub-basin under higher extension rates and subsequently propagated southwestward along narrow rifts between strong basement blocks.

Beyond the regional application to the SCS focused on in this study, our findings may have implications for a more generic understanding of V-shaped rift basins that develop far from rotation poles. An extension gradient appears as a necessary but not sufficient conditions for the development of V-shaped oceanic basins. Instead, the coupled effects of far-field tectonic forcing and inherited lithospheric heterogeneity causes localization of extension into narrow and deep rift segments preconditioning the lithosphere for the subsequent propagation of seafloor spreading exploiting the established gradients. These findings provide an important reference for refining current models and classifications of propagating rift systems worldwide.

Conflict of Interest

The authors declare no conflicts of interest for this study.

Data Availability Statement

All data, including 3D scanning datasets from the final experimental results (3D DEMs of surface deformation and the 2D DEM profiles extracted from western segment and eastern segment) and particle image velocimetry (PIV) products at four extension states (25 mm, 50 mm, 75 mm, and 100 mm), together with the plotting codes used to generate the figures, are available open access in (G. X. Yang et al., 2025b) provided by GFZ Data Services (https://doi.org/10.5880/fidgeo.2025.093)

Acknowledgments

We sincerely thank Reviewer Prokop Závada, the other anonymous reviewer, and the editors for their valuable and constructive comments, which have significantly contributed to the enhancement of our manuscript. We gratefully acknowledge the Key Laboratory of Reservoir Description, CNPC (Northwest Branch) and its 3D Dynamic Structural-Trap Analog Modeling Platform/Team for providing experimental facilities and technical support during the analogue modeling work. We also thank the HelTec -Laboratory for Experimental Tectonics at the GFZ German Research Centre for Geosciences for realizing conceptual pilot experiments and preliminary analysis. We are grateful to Claudio Faccenna for hosting Gengxiong Yang during her stay at GFZ in Potsdam, constructive discussions and insightful suggestions. We thank GFZ data services for publishing the data underlying this study. We thank Drs. Jun Liu, Jian Cui, Shaohang Yang, and Yuqi Zhu, as well as laboratory engineers Frank Neumann, Wenqiang Liu, and Wei Wang, for their experimental assistance and guidance. This work was jointly supported by the National Natural Science Foundation of China (Nos. 42372264, 41927802, 41972219), the National Science and Technology Major Project of China (Nos. 2016ZX05026-002-007, 2016ZX05003-001), and the China Scholarship Council (No. 202306190103).

References

Adam, J., Urai, J. L., Wieneke, B., Oncken, O., Pfeiffer, K., Kukowski, N., et al. (2005). Shear Localisation and Strain Distribution during Tectonic Faulting—New Insights from Granular-Flow Experiments and High-Resolution Optical Image Correlation Techniques. *Journal of Structural Geology*, *27* (2), 283–301. https://doi.org/10.1016/j.jsg.2004.08.008

Bai, Y., Wu, S., Liu, Z., Müller, R. D., Williams, S. E., Zahirovic, S., & Dong, D. (2015). Full-fit reconstruction of the South China Sea conjugate margins. *Tectonophysics*, *661*, 121–135. https://doi.org/10.1016/j.tecto.2015.08.028

Barckhausen, U., & Roeser, H. A. (2004). Seafloor spreading anomalies in the South China Sea revisited. In P. Clift (Ed.), Continent–Ocean Interactions in the East Asian Marginal Seas (121–125). *American Geophysical Union, Geophysical Monograph*, 149, 121-135. https://doi.org/10.1029/149GM07

Barckhausen, U., Engels, M., Franke, D., Ladage, S., & Pubellier, M. (2014). Evolution of the South China Sea: Revised ages for breakup and seafloor spreading. *Marine and Petroleum Geology*, *58*(B), 599–611. https://doi.org/10.1016/j.marpetgeo.2014.02.022

Briais, A., Patriat, P., & Tapponnier, P. (1993). Updated interpretation of magnetic anomalies and seafloor spreading stages in the South China Sea: Implications for the Tertiary Tectonics of Southeast Asia. *Journal of Geophysical Research: Solid Earth*, *98*, 6299–6328. https://doi.org/10.1029/92jb02280

Brun, J.-P. (2002). Deformation of the continental lithosphere: Insights from brittle–ductile models. *Geological Society, London, Special Publications*, *200*(1), 355–370. https://sp.lyellcollection.org/content/200/1/355

Brune, S., & Autin, J. (2013). The rift to break-up evolution of the Gulf of Aden: Insights from 3D numerical lithospheric-scale modelling. *Tectonophysics*, *607*, 65–79. https://doi.org/10.1016/j.tecto.2013.06.029

Brune, S., Heine, C., Pérez-Gussinyé, M., & Sobolev, S. V. (2014). Rift migration explains continental margin asymmetry and crustal hyper-extension. *Nature Communications, 5*, 4014. https://doi.org/10.1038/ncomms5014

Brune, S., Kolawole, F., Olive, J.-A., Stamps, D. S., Buck, W. R., Buiter, S. J. H., Furman, T., & Shillington, D. J. (2023). Geodynamics of continental rift initiation and evolution. *Nature Reviews Earth & Environment*, *4*(4), 235–253. https://doi.org/10.1038/s43017-023-00391-3

Cameselle, A. L., Ranero, C. R., & Barckhausen, U. (2020). Understanding the 3D formation of a wide rift: The central South China Sea rift system. *Tectonics*, *39*, e2019TC006040. https://doi.org/10.1029/2019TC006040

Cameselle, A.L., Ranero, C.R., Franke, D. & Barckhausen, U. (2017), The continent-ocean transition on the northwestern South China Sea. *Basin Research*, *29*, 73-95. https://doi.org/10.1111/bre.12137

Cheng, J. H., Zhang, J. Z., Zhao, M. H., Du, F., Fan, C. Y., Wang, X. Y., & Qiu, X. L. (2021). Spatial distribution and origin of the high-velocity lower crust in the northeastern South China Sea. *Tectonophysics*, *819*, 229086. https://doi.org/10.1016/j.tecto.2021.229086

Clift, P. D., & Sun, Z. (2006). The sedimentary and tectonic evolution of the Yinggehai-Song Hong Basin and the southern Hainan margin, South China Sea: Implications for Tibetan uplift and monsoon intensification. *Journal of Geophysical Research: Solid Earth*, *111*(B6), B06405. https://doi.org/10.1029/2005JB004048

Clift, P. D., Lin, J., & Barckhausen, U. (2002). Evidence of low flexural rigidity and low viscosity lower continental crust during continental break-up in the South China Sea. *Marine and Petroleum Geology*, *19*(8), 951–970. https://doi.org/10.1016/S0264-8172(02)00108-3

Clift, P. D., Lee, G. H., Anh Duc, N., Barckhausen, U., Van Long, H., and Zhen, S. (2008). Seismic reflection evidence for a dangerous grounds miniplate: no extrusion origin for the south china sea. *Tectonics*, *27*(3), TC3008. https://doi.org/10.1029/2007TC002216

Clifton, A. E., & Schlische, R. W. (2001). Nucleation, growth and linkage of faults in oblique rift zones: Results from experimental clay models and implications for maximum fault size. *Geology*, *29*(5), 455–458, https://doi.org/10.1130/0091-7613(2001)029<0455:NGALOF>2.0.CO;2.

Corti, G., Bonini, M., Sokoutis, D., Innocenti, F., Manetti, P., Cloetingh, S. A. P. L., and Mulugeta, G. (2004). Continental rift architecture and patterns of magma migration: A dynamic analysis based on centrifuge models. *Tectonics*, *23*(2), TC2012. https://doi.org/10.1029/2003TC001561

Corti, G. (2008). Control of rift obliquity on the evolution and segmentation of the main Ethiopian rift. *Nature Geoscience*, *1*(4), 258–262. https://doi.org/10.1038/ngeo160

Corti, G., van Wijk, J. W., Cloetingh, S. A. P. L., and Morley, C. K. (2007). Tectonic inheritance and continental rift architecture: Numerical and analogue models of the East African Rift system. *Tectonics*, *26*(6), TC6006. https://doi.org/10.1029/2006TC002086

Cullen, A., Reemst, P., Henstra, G., Gozzard, S., & Ray, A. (2010). Rifting of the South China Sea: New perspectives. *Petroleum Geoscience, 16*(3), 273–282. https://doi.org/10.1144/1354-079309-908

Deng, H. D., Ren, J. Y., Pang, X., Rey, P. F., McClay, K. R., Watkinson, I. M., Zheng, J. Y., & Luo, P. (2020). South China Sea documents the transition from wide continental rift to continental break up. *Nature Communications*, *11*, 4583. https://doi.org/10.1038/s41467-020-18448-y

Ding, W. W. (2021). Continental margin dynamics of South China Sea: From continental break-up to seafloor spreading (in Chinese with English abstract). *Earth Science*, *46*(3), 790–800. https://doi.org/10.3799/dqkx.2020.303

Ding, W. W, & Li, J. B. (2016). Propagated rifting in the southwest sub-basin, South China Sea: insights from analogue modelling. *Journal of Geodynamics*, *100*, 71-86. https://doi.org/10.1016/j.jog.2016.02.004

Ding, W. W., Franke, D., Li, J.-B., & Steuer, S. (2013). Seismic stratigraphy and tectonic structure from a composite multi-channel seismic profile across the entire Dangerous Grounds, South China Sea. *Tectonophysics, 582*, 162–176. https://doi.org/10.1016/j.tecto.2012.09.026

Ding, W. W., Schnabel, M., Franke, D., Ruan, A.-G., & Wu, Z.-L. (2012). Crustal structure across the northwestern margin of the South China Sea: Evidence for magma-poor rifting from a wide-angle seismic profile. *Acta Geologica Sinica - English Edition*, *86*(4), 854–866. https://doi.org/10.1111/j.1755-6724.2012.00711.x

Ding, W. W., Sun, Z., Dadd, K. A., Fang, Y., & Li, J. (2018). Structures within the oceanic crust of the central South China Sea basin and their implications for oceanic accretionary processes. *Earth and Planetary Science Letters, 488*, 115–125. https://doi.org/10.1016/j.epsl.2018.02.011

Ding, W. W., Sun, Z., Mohn, G., Nirrengarten, M., Tugend, J., Manatschal, G., and Li, J. B. (2020). Lateral evolution of the rift-to-drift transition in the South China Sea: Evidence from multi-channel seismic data and IODP Expeditions 367&368 drilling results. *Earth and Planetary Science Letters*, *531*, 115932. https://doi.org/10.1016/j.epsl.2019.115932

Duclaux, G., Huismans, R. S. & May, D. A. (2020). Rotation, narrowing, and preferential reactivation of brittle structures during oblique rifting. *Earth and Planetary Science Letters*, *531*, 115952. https://doi.org/10.1016/j.epsl.2019.115952.

Fan, J., Zhao, D., Dong, D., & Zhang, G. (2017). P-wave tomography of subduction zones around the central Philippines and its geodynamic implications. *Journal of Asian Earth Sciences*, *146*, 76–89. https://doi.org/10.1016/j.jseaes.2017.05.015

Franke, D., Savva, D., Pubellier, M., Steuer, S., Mouly, B., Auxiètre, J.-L., Méresse, F., and Chamot-Rooke, N. (2014). The final rifting evolution in the south china sea. *Marine and Petroleum Geology*, *58*, 704-720. https://doi.org/10.1016/j.marpetgeo.2013.11.020

Glerum, A., Brune, S., Stamps, D. S., & Strecker, M. R. (2020). Victoria continental microplate dynamics controlled by the lithospheric strength distribution of the East African Rift. *Nature Communications, 11*(1), 2881. https://doi.org/10.1038/s41467-020-16176-x

Gouiza, M., & Naliboff, J. (2021). Rheological inheritance controls the formation of segmented rifted margins in cratonic lithosphere. *Nature Communications*, *12*(1), 4653. https://doi.org/10.1038/s41467-021-24945-5

Hall, R. (2002). Cenozoic geological and plate tectonic evolution of SE Asia and the SW Pacific: Computer-based reconstructions, model and animations. *Journal of Asian Earth Sciences*, *20*(4), 353–431. https://doi.org/10.1016/S1367-9120(01)00069-4

Hall, R. (2012). Late Jurassic–Cenozoic reconstructions of the Indonesian region and the Indian Ocean. *Tectonophysics*, *570–571*, 1–41, https://doi.org/10.1016/j.tecto.2012.04.021

Han, J., Xu, G., Li, Y., & Zhuo, H. (2016). Evolutionary history and controlling factors of the shelf breaks in the Pearl River Mouth Basin, northern South China Sea. *Marine and Petroleum Geology*, *77*, 179–189. https://doi.org/10.1016/j.marpetgeo.2016.06.009

Hayes, D. E., & Nissen, S. S. (2005). The South China Sea margins: Implications for rifting contrasts. *Earth and Planetary Science Letters*, *237*(3–4), 601–616. https://doi.org/10.1016/j.epsl.2005.06.017

Heron, P. J., Pysklywec, R. N., & Stephenson, R. (2016). Lasting mantle scars lead to perennial plate tectonics. *Nature Communications*, *7*(1), 11834. https://doi.org/10.1038/ncomms11834

Holloway, N. (1982). North Palawan block, Philippines—Its relation to Asian mainland and role in evolution of South China Sea. *AAPG Bulletin*, *66*(9), 1355–1383. https://doi.org/10.1306/03B5A0BC-16D1-11D7-8645000102C1865D

Hubbert, M. K. (1937). Theory of scale models as applied to the study of geologic structures. *Geological Society of America Bulletin*, *48*(10), 1459–1520. https://doi.org/10.1130/GSAB-48-1459

Huismans, R. S., & Beaumont, C. (2002). Asymmetric lithospheric extension: The role of frictional plastic strain softening inferred from numerical experiments. *Geology*, *30*(3), 211–214. https://doi.org/10.1130/0091-7613(2002)030

Huismans, R. S., & Beaumont, C. (2011). Depth-dependent extension, two-stage breakup and cratonic underplating at rifted margins. *Nature, 473*(7345), 74–78. https://doi.org/10. 1038/nature09988

Huismans, R. S., & Beaumont, C. (2014). Rifted continental margins: The case for depth-dependent extension. *Earth and Planetary Science Letters*, *407*, 148–162. https://doi.org/10.1016/j.epsl.2014.09.032

Hutchison, C. S. (2004). Marginal basin evolution: The southern South China Sea. *Marine and Petroleum Geology*, *21*(9), 1129–1148. https://doi.org/10.1016/j.marpetgeo.2004.07.002

Jiang, H., Huang, H. B., He, E. Y., Guo, J., & Qiu, X. L. (2025). Hydration in the crust and upper mantle near the extinct spreading ridge in the eastern sub-basin, South China Sea. *Geophysical Research Letters*, *52*, e2025GL115670. https://doi.org/10.1029/2025GL115670

Johnson, H. P., & Carlson, R. L. (1992). Variations of sea floor depth with age: A test of models based on drilling results. *Geophysical Research Letters, 19*(19), 1971–1974. https://doi.org/10.1029/92GL02182

Koyi, H. A. (1997). Analogue modelling: From a qualitative to a quantitative technique—A historical outline. *Journal of Petroleum Geology*, *20*(2), 223–238. https://doi.org/10.1111/j.1747-5457.1997.tb00774.x

Larvet, T., Le Pourhiet, L., Pubellier, M., & Gyomlai, T. (2023). Slab pull driven South China Sea opening implies a Mesozoic Proto South China Sea. *Geophysical Research Letters*, *50*, e2023GL105292. https://doi.org/10.1029/2023GL105292

Le Pourhiet, L., Chamot-Rooke, N., Delescluse, M., May, D. A., Watremez, L., & Pubellier, M. (2018). Continental break-up of the South China Sea stalled by far-field compression. *Nature Geoscience*, *11*(8), 605–609. https://doi.org/10.1038/s41561-018-0178-5

Le Pourhiet, L., May, D. A., Huille, L., Watremez, L., & Leroy, S. (2017). A genetic link between transform and hyper-extended margins. *Earth and Planetary Science Letters*, *465*, 184–192. https://doi.org/10.1016/j.epsl.2017.02.043

Lee, T.-Y., & Lawver, L. A. (1995). Cenozoic plate reconstruction of Southeast Asia. *Tectonophysics*, *251*(1–4), 85–138. https://doi.org/10.1016/0040-1951(95)00023-2

Li, C. F., Li, J. B., Ding, W. W., & Franke, D. (2015). Seismic stratigraphy of the central South China Sea basin and implications for neotectonics. *Journal of Geophysical Research: Solid Earth*, *120*(3): 1377-139. https://doi.org/10.1002/2014JB011686.

Li, C. F., Xu, X., Lin, J., Sun, Z., Zhu, J., Yao, Y. J., et al. (2014). Ages and magnetic structures of the South China Sea constrained by deep tow magnetic surveys and IODP Expedition 349. *Geochemistry, Geophysics, Geosystems*, *15*(12), 4958–4983. https://doi.org/10.1002/2014GC005567

Li, F. C., Sun, Z., Yang, H. F., Lin, J., Stock, J. M., Zhao, Z. X., Xu, H. H., & Sun, L. T. (2020). Continental Interior and Edge Breakup at Convergent Margins Induced by Subduction Direction Reversal: A Numerical Modeling Study Applied to the South China Sea Margin. *Tectonics*, *39*(11), e2020TC006409. https://doi.org/10.1029/2020TC006409

Li, F. C., Sun, Z., & Yang, H. F. (2018). Possible spatial distribution of the Mesozoic volcanic arc in the present-day South China Sea continental margin and its tectonic implications. *Journal of Geophysical Research: Solid Earth*, *123*, 6215–6235. https://doi.org/10.1029/2017JB014861

Li, F. C, Sun, Z., Pang, X., Liao, J., Yang, H. F., Xie, H., Zhuo, H. T., & Zhao, Z. X. (2019). Low-viscosity crustal layer controls the crustal architecture and thermal distribution at hyperextended margins: Modeling insight and application to the northern South China Sea margin. *Geochemistry, Geophysics, Geosystems*, *20*(7), 3248–3267. https://doi.org/10.1029/2019GC008200

Li, H. L., Wu, Z. C., Ji, F., Gao, J. Y., Yang, C. G., Yuan, Y., Xu, M. J., & Zhang, J. L. (2020). Crustal density structure of the northern South China Sea from constrained 3-D gravity inversion. *Chinese Journal of Geophysics*, *63*(5), 1894–1912. https://doi.org/10.6038/cjg2020N0064

Li, J. B., Ding, W. W., Gao, J. Y., Wu, Z. Y., & Zhang, J. (2011). Cenozoic evolution model of the sea-floor spreading in South China Sea: New constraints from high resolution geophysical data. *Chinese Journal of Geophysics, 54*(6), 894–906. https://doi.org/10.1002/cjg2.1672

Li, J. B., Ding, W. W., Wu, Z. Y., Zhang, J., & Dong, C. Z. (2012). The propagation of seafloor spreading in the southwestern subbasin, South China Sea. *Chinese Science Bulletin*, *57*(24), 3182–3191. https://doi.org/10.1007/s11434-012-5329-2

Li, Y., Huang, H., Grevemeyer, I., Qiu, X., Zhang, H., & Wang, Q. (2021). Crustal structure beneath the Zhongsha Block and the adjacent abyssal basins, South China Sea: New insights into rifting and initiation of seafloor spreading. *Gondwana Research, 99*, 53–76. https://doi.org/10.1016/j.gr.2021.06.009

Lin, Z., Xiao, Z., Zhang, Y., Zhou, Y., Lin, J., Wang, J., Yan, C., & Xu, M. (2025). Lithospheric footprint of mantle upwelling beneath late Cenozoic basalts in the Beibu Gulf Basin, northwestern South China Sea. *Journal of Geophysical Research: Solid Earth*, *130*(6), e2024JB030379. https://doi.org/10.1029/2024JB030379

Liu, J. B., Sun, Z., Wang, Z. F., Sun, Z. P., Zhao, Z. X., Wang, Z. W., et al. (2015). Tectonic differences between eastern and western sub-basins of the Qiongdongnan Basin and their dynamics. *Marine Geophysical Researches*, *36*(1), 61–79. https://doi.org/10.1007/s11001-014-9247-3

Liu, J., Rosenau, M., Brune, S., Kosari, E., Rudolf, M., & Oncken, O. (2024). Fault networks in triaxial tectonic settings: Analog modeling of distributed continental extension with lateral shortening. *Tectonics*, *43*, e2023TC008127. https://doi.org/10.1029/2023TC008127

Luo, P., Manatschal, G., Ren, J. Y., Zhao, Z. X., Wang, H. J., & Tong, D. J. (2021). Tectono-magmatic and stratigraphic evolution of final rifting and breakup: Evidence from the tip of the southwestern propagator in the South China Sea. *Marine and Petroleum Geology, 129*, 105079. https://doi.org/10.1016/j.marpetgeo.2021.105079

Madon, M., Kim, C. L., & Wong, R. (2013). The structure and stratigraphy of deepwater Sarawak, Malaysia: Implications for tectonic evolution. *Journal of Asian Earth Sciences, 76*, 312–333. https://doi.org/10.1016/j.jseaes.2013.04.040

Maestrelli, D., Montanari, D., Corti, G., Del Ventisette, C., Moratti, G., & Bonini, M. (2020). Exploring the interactions between rift propagation and inherited crustal fabrics through experimental modeling. *Tectonics*, *39*(12), e2020TC006211. https://doi.org/10.1029/2020TC006211

Mazur, S., Green, C., Stewart, M.G., Whittaker, J.M., Williams, S. & Bouatmani, R. (2012). Displacement along the Red River Fault constrained by extension estimates and plate reconstructions. *Tectonics*, *31*(5), TC5008. https://doi.org/10.1029/2012TC003174

McClay, K. R., & White, M. J. (1995). Analogue modelling of orthogonal and oblique rifting. *Marine and Petroleum Geology, 12*(2), 137–151. https://doi.org/10.1016/0264-8172(95)92835-K

McKenzie, D. (1978). Some remarks on the development of sedimentary basins. *Earth and Planetary Science Letters, 40*(1), 25–32. https://doi.org/10.1016/0012-821X(78)90071-7

Molnar, N. E., Cruden, A. R., & Betts, P. G. (2017). Interactions between propagating rotational rifts and linear rheological heterogeneities: Insights from three-dimensional laboratory experiments. *Tectonics*, *36*, 420–443. https://doi.org/10.1002/2016TC004447

Molnar, N., Cruden, A., & Betts, P. (2020). The role of inherited crustal and lithospheric architecture during the evolution of the Red Sea: insights from three-dimensional analogue experiments. *Earth and Planetary Science Letters*, *544*, 116377. https://doi.org/10.1016/j.epsl.2020.116377

Mondy, L. S., Rey, P. F., Duclaux, G., & Moresi, L. (2018). The role of asthenospheric flow during rift propagation and breakup. *Geology, 46*(2), 103–106. https://doi.org/10.1130/G39674.1

Morley, C. K. (2012). Late Cretaceous-Early Palaeogene tectonic development of SE Asia. *Earth-Science Reviews*, *115*(1–2), 37–75. https://doi.org/10.1016/j.earscirev.2012.08.002

Pérez-Gussinyé, M., Morgan, J. P., Reston, T. J., & Ranero, C. R. (2006). The rift-to-drift transition at non-volcanic margins: Insights from numerical modelling. *Earth and Planetary Science Letters, 244*(1–2), 458–473. https://doi.org/10.1016/j.epsl.2006.01.059

Pérez-Gussinyé, M., Xin, Y., Cunha, T., Ram, R., Andrés-Martínez, M., Dong, D., & García-Pintado, J. (2024). Synrift and post-rift thermal evolution of rifted margins: A re-evaluation of classic models of extension. *Geological Society, London, Special Publications*, *547*(1), 13–38. https://doi.org/10.1144/SP547-2023-128

Pichot, T., Delescluse, M., Chamot-Rooke, N., Pubellier, M., Qiu, Y., Meresse, F., et al. (2014). Deep crustal structure of the conjugate margins of the SW South China Sea from wide-angle refraction seismic data. *Marine and Petroleum Geology*, *58*, 627–643. https://doi.org/10.1016/j.marpetgeo.2013.10.008

Pubellier, M., Chang, S.-P., & Delescluse, M. (2022). The South China Sea–Rifting and the evolution of a marginal basin. In G. Peron-Pinvidic (Ed.), *Continental Rifted Margins 2* (Chapter 5), 107–131. Wiley. https://doi.org/10.1002/9781119986959.ch5

Qing, J., Liao, J., & Brune, S. (2024). Rift propagation interacting with pre-existing microcontinental blocks. *Journal of Geophysical Research: Solid Earth, 129*, e2023JB028109. https://doi.org/10.1029/2023JB028109

Qiu, X. L., Ye, S. Y., Wu, S. M., Shi, X. B., Zhou, D., Xia, K. Y., & Flueh, E. R. (2001). Crustal structure across the Xisha Trough, northwestern South China Sea. *Tectonophysics, 341*(1–4), 179–193. https://doi.org/10.1016/S0040-1951(01)00222-0

Qiu, X. L., Zhao, M. H., Ao, W., Lv, C. C., Hao, T. Y., You, Q. Y., Ruan, A. G., & Li, J. B. (2011). OBS survey and crustal structure of the southwest sub basin and Nansha Block, South China Sea. *Chinese Journal of Geophysics*, *54*(12), 3117–3128. https://doi.org/10.3969/j.issn.0001-5733.2011.12.012

Ranero, C. R., & Pérez-Gussinyé, M. (2010). Sequential faulting explains the asymmetry and extension discrepancy of conjugate margins. *Nature*, *468*(7321), 294–299. https://doi.org/10.1038/nature09520

Reber, J. E., Cooke, M. L., & Dooley, T. P. (2020). What model material to use? A review on rock analogs for structural geology and tectonics. *Earth-Science Reviews, 202*, 103107. https://doi.org/10.1016/j.earscirev.2020.103107

Savva, D., Pubellier, M., Franke, D., Chamot-Rooke, N., Méresse, F., Steuer, S., & Auxiètre, J.-L. (2014). Different expressions of rifting on the South China Sea margins. *Marine and Petroleum Geology*, *58*, 579–598. https://doi.org/10.1016/j.marpetgeo.2014.05.023

Sibuet, J.-C., Yeh, Y.-C., & Lee, C.-S. (2016). Geodynamics of the South China Sea. *Tectonophysics*, *692*, 98–119. https://doi.org/10.1016/j.tecto.2016.02.022

Shi, X., Kohn, B., Spencer, S., Guo, X., Li, Y., Yang, X., Shi, H., & Gleadow, A. (2011). Cenozoic denudation history of southern Hainan Island, South China Sea: Constraints from low-temperature thermochronology. *Tectonophysics, 504*(1–4), 100–115. https://doi.org/10.1016/j.tecto.2011.03.006

Sokoutis, D., & Willingshofer, E. (2011). Decoupling during continental collision and intra-plate deformation. *Earth and Planetary Science Letters*, *305*, 435–444. https://doi.org/10.1016/j.epsl.2011.03.028

Sun, Z., Lin, J., Qiu, N., Jian, Z. M., Wang, P. X., Pang, X., Zheng, J. Y., & Zhu, B. D. (2019). The role of magmatism in thinning and breakup of the South China Sea continental margin. *National Science Review*, *6*(5), 871–876. https://doi.org/10.1093/nsr/nwz116

Sun, Z., Zhong, Z., Keep, M., Zhou, D., Cai, D., Li, X., Wu, S., & Jiang, J. (2009). 3D analogue modeling of the South China Sea: A discussion on breakup pattern. *Journal of Asian Earth Sciences,* *34*(4), 544–556. https://doi.org/10.1016/j.jseaes.2008.09.002

Sun, Z., Zhou, D., Zeng, Z. X., & Zhong, Z. H. (2000). Summary on analogue modeling of continental rifting. *Geological Science and Technology Information*, *19*(1), 23–26.

Tang, X. Y., Chen, L., Hu, S. B., Yang, S. H., Zhang, G. C., Shen, H. L., Rao, S., & Li, W. W. (2014). Tectono-thermal evolution of the Reed Bank Basin, Southern South China Sea. *Journal of Asian Earth Sciences*, *96*, 344–352. https://doi.org/10.1016/j.jseaes.2014.09.030.

Tetreault, J. L. & Buiter, S. J. H. (2018). The influence of extension rate and crustal rheology on the evolution of passive margins from rifting to break-up. *Tectonophysics*, *746*(30), 155-172. https://doi.org/10.1016/j.tecto.2017.08.029

Van Wijk, J. W., & Blackman, D. K. (2005). Dynamics of continental rift propagation: the end-member modes, *Earth and Planetary Science Letters*, *229* (3–4), 247–258. https://doi.org/10.1016/j.epsl.2004.10.039.

Wang, P., Li, S., Suo, Y., Guo, L., Santosh, M., Li, X., et al. (2021). Structural and kinematic analysis of Cenozoic rift basins in the South China Sea: A synthesis. *Earth-Science Reviews, 216,* 103522. https://doi.org/10.1016/j.earscirev.2021.103522

Wang, W., Prada, M., Cameselle, A., Grevemeyer, I., Barckhausen, U., Dong, D., & Ranero, C. R. (2025). Mode of extension during the Xisha Trough rift in the South China Sea. *Journal of Geophysical Research: Solid Earth*, *130*(7), e2024JB030564. https://doi.org/10.1029/2024JB030564

Wang, Z., Ren, J., Hu, C., & Xu, Y. (2025). Differential extrusion of Indochina South China block and its interplay with slab pull tectonics: Evidence for end Oligocene basin inversion in the Beibuwan Basin. *Tectonics*, *44*(1), e2024TC008326. https://doi.org/10.1029/2024TC008326

Wei, X. D., Ruan, A. G., Ding, W. W., Wu, Z. C., Dong, C., Zhao, Y. H. (2020). Crustal structure and variation in the southwest continental margin of the South China

Sea: Evidence from a wide-angle seismic profile. *Journal of Asian Earth Sciences*, *203*, 104557. https://doi.org/10.1016/j.jseaes.2020.104557

Weijermars, R., & Schmeling, H. (1986). Scaling of Newtonian and non-Newtonian fluid dynamics without inertia for quantitative modelling of rock flow due to gravity (including the concept of rheological similarity). *Physics of the Earth and Planetary Interiors*, *43*(4), 316–330. https://doi.org/10.1016/0031-9201(86)90021-X

Wu, J., & Suppe, J. (2018). Proto-South China Sea plate tectonics using subducted slab constraints from tomography. *Journal of Earth Science*, 29(6), 1304–1318. https://doi.org/10.1007/s12583-017-0813-x

Xia, Z. Y., Wan, Z. F., Wang, X. Q., Shi, Q. H., Cai, S., & Xia, B. (2016). The tectonic differences between the east and the west in the deep-water area of the northern South China Sea. *Acta Oceanologica Sinica, 35*(1), 86–95. https://doi.org/10.1007/s13131-016-0799-8

Xie, X. N., Ren, J. Y., Wang, Z. F., Li, X. S., & Lei, C. (2015). Difference of tectonic evolution of continental marginal basins of South China Sea and relationship with SCS spreading(in Chinese with English abstract). *Earth Science Frontiers, 22*(1), 77–87. https://doi.org/10.13745/j.esf.2015.01.007

Xu, Y. C., Ren, J. Y., Zhao, Y. H., Zheng, J. Y., Lei, C., & Zhu, D. W. (2024). Consequences of continental core complexes on rifting patterns: Insights from multichannel seismic data from the northern margin of the South China Sea. *Tectonics*, *43*(4), e2023TC007870. https://doi.org/10.1029/2023TC007870

Yan, P., & Liu, H. L. (2004). Tectonic-stratigraphic division and blind fold structures in Nansha waters, South China Sea. *Journal of Asian Earth Sciences, 24*(3), 337–348. https://doi.org/10.1016/j.jseaes.2003.11.001

Yan, P., Wang, L., & Wang, Y. (2014). Late Mesozoic compressional folds in Dongsha Waters, the northern margin of the South China Sea. *Tectonophysics*, *615*, 213–223. https://doi.org/10.1016/j.tecto.2014.01.009

Yan, P., Zhou, D., & Liu, Z. (2001). A crustal structure profile across the northern continental margin of the South China Sea. *Tectonophysics*, *338*(1), 1–21. https://doi.org/10.1016/S0040-1951(01)00062-2

Yan, Q. S., Shi, X. F., & Castillo, P. (2014). The late Mesozoic–Cenozoic tectonic evolution of the South China Sea: A petrologic perspective. *Journal of Asian Earth Sciences, 85*, 178–201. https://doi.org/10.1016/j.jseaes.2014.02.003

Yang, G. X., Yin, H. W., Schiffer, C., Brune, S., Jia, D., & Wang, W. (2025a). Crustal heterogeneity controls the along-strike segmentation: Analog and numerical models of the northern South China Sea. *Tectonics*, *44*, e2024TC008541. https://doi.org/10.1029/2024TC008541

Yang, G. X. Rosenau, M., Yin, H. W., Pan, S. X., Pei, Y. W. (2025b). Datasets of analog modeling results for the V-shaped opening of the South China Sea: 3D DEMs and PIV results [Dataset]. GFZ Data Services. https://doi.org/10.5880/fidgeo.2025.093

Yang, H. B, Guan, H. X., Geoffroy, L., Chen, H. L., Zhao, M. H., & Xu, M. (2025). Syn-rift margin architecture influenced by surficial loads. *Earth and Planetary Science Letters*, *671*, 119637. https://doi.org/10.1016/j.epsl.2025.119637

Ye, Q., Mei, L., Shi, H., Camanni, G., Shu, Y., & Wu, J. (2018). The Late Cretaceous tectonic evolution of the South China Sea area: An overview, and new perspectives from 3D seismic reflection data. *Earth-Science Reviews*, *187*, 186–204. https://doi.org/10.1016/j.earscirev.2018.09.013

Ye, Q., Mei, L., Shi, H., Du, J., Deng, P., Shu, Y., & Camanni, G. (2020). The influence of pre-existing basement faults on the Cenozoic structure and evolution of the proximal domain, northern South China Sea rifted margin. *Tectonics*, *39*(3). https://doi.org/10.1029/2019TC005845

Yu, X., & Liu, Z. (2020). Non-mantle-plume process caused the initial spreading of the South China Sea. *Scientific Reports*, *10*, 8500. https://doi.org/10.1038/s41598-020-65174-y

Zahirovic, S., Seton, M., & Müller, R. D. (2014). The Cretaceous and Cenozoic tectonic evolution of Southeast Asia. *Solid Earth*, *5*(1), 227–273. https://doi.org/10.5194/se-5-227-2014

Zhang, C. L., Xia, S. H., Cao, J. H., Fan, C. Y., Wan, K. Y., & Gou, T. (2025). Control of coral reefs formation by boudin-like crustal extension processes in the South China Sea: New insights from wide-angle seismic imaging. *Journal of Geophysical Research: Solid Earth*, *130*, e2024JB030150. https://doi.org/10.1029/2024JB030150

Zhang, J. Y., Zhao, M. H., Sun, Z., Sun, L. T., Xu, M., Yang, H. F., et al. (2023). Large volume of magma involved in South China Sea rifting: Implication for mantle breakup earlier than crust. *Tectonophysics*, *853*, 229801. https://doi.org/10.1016/j.tecto.2023.229801

Zhang, J., Xiong, L.-P., & Wang, J.-Y. (2001). The characteristics and mechanism of geodynamic evolution of the South China Sea. *Chinese Journal of Geophysics*, *44*(5), 602–610. https://doi.org/10.1002/cjg2.179

Zhang, J. Z, Li, Y. H., Yao, Y. J., Zhao, M. H., Grevemeyer, I., Sallares, V., et al. (2025). Seismic structure and the variation of magmatic budget in the southwest sub-basin of the South China Sea. *Journalof Geophysical Research: Solid Earth*, *130*(8), e2025JB031304. https://doi.org/10.1029/2025JB031304

Zhang, Y. F., Sun, Z., Zhang, J. Y., & Wang, L. J. (2020). The structure, depositional style and accumulation characteristics of continental margin with diachronous breakup in the northern South China Sea. *International Geology Review, 62*(7–8), 1006–1018. https://doi.org/10.1080/00206814.2019.1631219

Zhao, M., He, E. Y., Sibuet, J.-C., Sun, L. T., Qiu, X., Tan, P. C., & Wang, J. (2018). Postseafloor spreading volcanism in the central East Sub-basin of the South China Sea. *Geochemistry, Geophysics, Geosystems*, *19*(3), 621–641. https://doi.org/10.1002/2017GC007034

Zhao, F., Alves, T. M., Xia, S. H., Li, W., Wang, L., Mi, L. J., et al. (2019). Along-strike segmentation of the South China Sea margin imposed by inherited pre-rift basement structures. *Earth and Planetary Science Letters*, *530*, 115862. https://doi.org/10.1016/j.epsl.2019.115862

Zhou, D., Sun, Z., Chen, H. Z., & Qiu, Y. X. (2005). Mesozoic lithofacies, paleo-geography, and tectonic evolution of the South China Sea and surrounding areas. *Earth Science Frontiers*, *12*(3), 204–218.

Zulauf, J., & Zulauf, G. (2004). Rheology of plasticine used as rock analogue: The impact of temperature, composition and strain. *Journal of Structural Geology*, *26*(4), 725–737. https://doi.org/10.1016/j.jsg.2003.07.005

Zulauf, J., Zulauf, G., Steenken, A., & Craemer, C. (2011). Results from experiments using power–law rock analogs. *Tectonophysics, 503*(1–2), 106–116. https://doi.org/10.1016/j.tecto.2010.09.016

Zwaan, F., & Schreurs, G. (2023). Analog models of lithospheric-scale rifting monitored in an X-ray CT scanner. *Tectonics*, *42*(3), e2022TC007291. https://doi.org/10.1029/2022TC007291

Zwaan, F., Chenin, P., Erratt, D., Manatschal, G., & Schreurs, G. (2021). Complex rift patterns, a result of interacting crustal and mantle weaknesses, or multiphase rifting? Insights from analogue models. *Solid Earth*, *12*(7), 1473–1495.

https://doi.org/10.5194/se-12-1473-2021

Zwaan, F., Chenin, P., Erratt, D., Manatschal, G., & Schreurs, G. (2022). Competition between 3D structural inheritance and kinematics during rifting: Insights from analogue models. *Basin Research*, *34*(2), 824–854. https://doi.org/10.1111/bre.12642

Zwaan, F., Schreurs, G., & Buiter, S. J. H. (2019). A systematic comparison of experimental set-ups for modelling extensional tectonics. *Solid Earth*, *10*(4), 1063–1097. https://doi.org/10.5194/se-10-1063-2019

Zwaan, F., Schreurs, G., & Rosenau, M. (2020). Rift propagation in rotational versus orthogonal extension: Insights from 4D analogue models. *Journal of Structural Geology*, 135, 103946. https://doi.org/10.1016/j.jsg.2019.103946